

A Viscoelastic Earthquake Simulator with Application to the San Francisco Bay Region

by Fred F. Pollitz

Abstract Earthquake simulation on synthetic fault networks carries great potential for characterizing the statistical patterns of earthquake occurrence. I present an earthquake simulator based on elastic dislocation theory. It accounts for the effects of interseismic tectonic loading, static stress steps at the time of earthquakes, and post-earthquake stress readjustment through viscoelastic relaxation of the lower crust and mantle. Earthquake rupture initiation and termination are determined with a Coulomb failure stress criterion and the static cascade model. The simulator is applied to interacting multifault systems: one, a synthetic two-fault network, and the other, a fault network representative of the San Francisco Bay region. The faults are discretized both along strike and along dip and can accommodate both strike slip and dip slip. Stress and seismicity functions are evaluated over 30,000 yr trial time periods, resulting in a detailed statistical characterization of the fault systems. Seismicity functions such as the coefficient of variation and a - and b -values exhibit systematic patterns with respect to simple model parameters. This suggests that reliable estimation of the controlling parameters of an earthquake simulator is a prerequisite to the interpretation of its output in terms of seismic hazard.

Introduction

Earthquake occurrence is to a large extent controlled by the evolution of crustal stress. This is supported by numerous studies of static stress triggering, as well as the existence of a persistent stress shadow (inhibition of earthquakes) following the 1906 earthquake (Stein, 1999). Long-term seismicity rates, fault interactions, and patterns of moderate to large earthquakes are products of models of fault systems controlled by the mechanics of crustal deformation over long time periods (Ward and Goes, 1993; Rundle *et al.*, 2005, 2006a). Understanding how such systems evolve in time under a relevant set of governing physical laws is a needed critical step toward reliable earthquake forecasting. Our understanding of the mechanics of crustal deformation has advanced to the point where we may address the issues relevant to probabilistic seismic hazard analysis (PSHA) with numerical simulations of seismicity.

An earthquake simulator essentially provides a means of tracking the increasing tectonic stress as it loads the faults, determines when a rupture initiates on one or more faults, how much and where a fault slips in an earthquake, and how stress is redistributed among the network faults as the result of an earthquake. Existing algorithms demonstrate the great potential of earthquake simulators for quantifying aspects of earthquake occurrence that are traditionally based on fragmentary geologic information or simply expert opinion. This includes the measures of coefficient of variation (COV), the

triggering capability of moderate earthquakes, and the likelihood of earthquakes rupturing through fault segment boundaries. In the context of elastic dislocation theory, Richards–Dinger and Dieterich (2007) have implemented an earthquake simulator on single-fault and multifault networks that accounts for rate-and-state friction effects during both the coseismic and interseismic time periods, as well as static stress steps; the same physics also determines the initiation and termination of ruptures. Ward (2000) and Rundle *et al.* (2006b) have implemented a large network of interacting faults in California that accounts for interseismic loading controlled by known fault slip rates, as well as static stress steps; they determine the initiation and termination of earthquake ruptures through a Coulomb failure stress criterion combined with a static cascade model. Although recognized as an important ingredient, none of the existing approaches account for viscoelastic stress transfer.

In this article I present an algorithm for generating synthetic seismicity in a fault network that includes the following elements (Fig. 1): (1) tectonic loading of a plate boundary zone, (2) coseismic stress steps at the time of earthquakes, and (3) viscoelasticity, through which stress is redistributed during interseismic time intervals through relaxation of the ductile lower crust and mantle. Earthquake ruptures are approximated using the static cascade model. All elements are

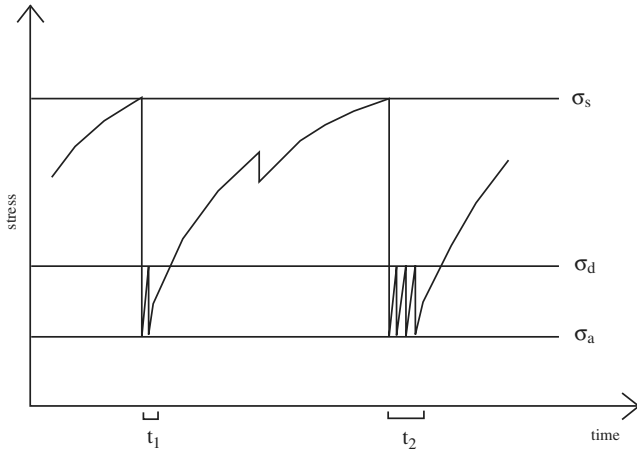


Figure 1. Stress history of a patch that had a slip event at times t_1 and t_2 . An event is initiated when stress attains the static frictional stress σ_s . The fault patch slips the amount necessary to reduce its stress to the arrest stress level σ_a in isolation. During an event, if stress on the same patch attains the dynamic friction value σ_d , it will slip again an amount necessary to reduce its stress to σ_a . Immediately after an event, the final stress may be different from σ_a because of the interaction of neighboring fault patches. The slippage during events at times t_1 and t_2 is not of finite duration (as depicted) but occurs instantaneously in the static cascade model. During the interseismic period the patch stressing rate will depart from linearity because of crust and mantle viscoelastic relaxation, and stress steps between slip events may arise from slip events on neighboring faults.

implemented in an interacting multifault network discretized both along strike and along dip.

With this simulator we may address many outstanding questions in PSHA. For example, what factors control COV and interaction probabilities (e.g., triggering capability of moderate earthquakes) on individual faults? How do these measures vary from fault to fault? What role does stress transfer play in shaping seismicity patterns on individual faults? How sensitive are these patterns to viscoelastic stress transfer? Do ruptures tend to initiate in the deeper crust and propagate upward?

Stress Evolution in a Viscoelastic Coupling Model

Pollitz and Schwartz (2008) developed expressions for stress evolution in a viscoelastic system where rupture of a given fault is periodic with identical slip in each event. We follow their development but drop the requirement that the ruptures occur periodically; in the present treatment, rupture of a given fault patch need only occur with a mean definite slip rate. Stress accumulated at point \mathbf{r} up to time t starting from a time t_0 is a combination of accumulated coseismic stress, postseismic stress, and background loading:

$$\sigma(\mathbf{r}, t) = \sigma(\mathbf{r}, t_0) + \sum_i [\sigma_{\text{co}}^{(i)}(\mathbf{r}, t) t_{i_0}^i] + \sum_i [\sigma_{\text{ps}}^{(i)}(\mathbf{r}, t) t_{i_0}^i] + \dot{\sigma}_{\text{load}}(\mathbf{r}) \times (t - t_0), \quad (1)$$

where accumulated coseismic and postseismic stress in a time interval (t_1, t_2) are, respectively,

$$\sigma_{\text{co}}^{(i)}(\mathbf{r}, t)|_{t_1}^{t_2} = \sum_{n=1}^{\infty} \sum_{jk} \int m_{jk}^{(i)(n)}(\mathbf{r}_0) \Psi_{jk}(\mathbf{r}, \mathbf{r}_0, 0^+) \{H[t - t^{(i)(n)}]|_{t_1}^{t_2} d^2\mathbf{r}_0, \quad (2)$$

$$\sigma_{\text{ps}}^{(i)}(\mathbf{r}, t)|_{t_1}^{t_2} = \sum_{n=1}^{\infty} \sum_{jk} \int m_{jk}^{(i)(n)}(\mathbf{r}_0) \{[\Psi_{jk}(\mathbf{r}, \mathbf{r}_0, t - t^{(i)(n)}) - \Psi_{jk}(\mathbf{r}, \mathbf{r}_0, 0^+)] \times H(t - t^{(i)(n)})\}|_{t_1}^{t_2} d^2\mathbf{r}_0. \quad (3)$$

In equations (1)–(3)

$t^{(i)(n)}$ = occurrence time of the n th event on fault i .

$m_{jk}^{(i)(n)}(\mathbf{r}_0)$ = jk moment tensor density component of the n th event at point \mathbf{r}_0 on fault i .

$\Psi_{jk}(\mathbf{r}, \mathbf{r}_0, t)$ = Green's function for the accumulated stress at point \mathbf{r} and time t in the viscoelastic system arising from the unit jk -component moment tensor source applied at point \mathbf{r}_0 and time 0. The use of linear viscoelasticity allows Ψ to be defined independently of the stress state, so that there is no nonlinear interaction between the loading and postseismic stress fields. The stress can be a linear combination of stress tensor components evaluated at \mathbf{r} , for example, the Coulomb stress function.

$H(t)$ = Heaviside step function.

$\dot{\sigma}_{\text{load}}$ = background loading rate.

Note that any of the above stress quantities is meant to be one of the components of a stress tensor σ , for example, $\sigma_{\alpha\beta}$, in which case the notation $\Psi_{jk\alpha\beta}$ for the Green's function would be appropriate. We omit these subscripts until Earthquake Simulation, where the full tensor notation is needed.

Loading rate is prescribed as

$$\dot{\sigma}_{\text{load}}(\mathbf{r}) = -\langle [\dot{\sigma}_{\text{co}}^{(i)}(\mathbf{r}, t) + \dot{\sigma}_{\text{ps}}^{(i)}(\mathbf{r}, t)_0^T] \rangle, \quad 4$$

where the dot superscript denotes time differentiation and $\langle \rangle$ denotes time average. Hence,

$$\begin{aligned} \dot{\sigma}_{\text{load}}(\mathbf{r}) &= -\lim_{T \rightarrow \infty} \frac{1}{T} [\sigma_{\text{co}}^{(i)}(\mathbf{r}, t)_0^T + \sigma_{\text{ps}}^{(i)}(\mathbf{r}, t)_0^T] \\ &= \lim_{T \rightarrow \infty} \frac{1}{T} \sum_i \sum_{n=1}^{\infty} \sum_{jk} \int m_{jk}^{(i)(n)}(\mathbf{r}_0) \\ &\quad \times \{ \Psi_{jk}[\mathbf{r}, \mathbf{r}_0, T - t^{(i)(n)}] H[T - t^{(i)(n)}] \\ &\quad - \Psi_{jk}[\mathbf{r}, \mathbf{r}_0, -t^{(i)(n)}] H[-t^{(i)(n)}] \} d^2\mathbf{r}_0. \end{aligned} \quad (5)$$

The time interval $(0, T)$ in equation (5) is an arbitrarily chosen time interval, which, through the n -summation, samples both past events ($t^{(i)(n)} < 0$) and future events ($t^{(i)(n)} > 0$). This definition is consistent with the loading rate given by equation (4) of Pollitz and Schwartz (2008) for the case of uniform recurrence intervals and identical slip per event.

The present definition is more general and ensures that, on average, coseismic stress changes negate the buildup of stress during interseismic times, so that the long-term stressing rate at a given point tends to zero. We may evaluate equation (4) by dividing the events into three groups. Let $S_1^{(i)}(T)$ be the set of events such that $0 < t^{(i)(n)} \leq T$; let $S_2^{(i)}(T)$ be the set of events such that $-T < t^{(i)(n)} \leq 0$; let $S_3^{(i)}(T)$ be the set of events such that $t^{(i)(n)} \leq -T$. The n sums in equation (5) can be regrouped as follows:

$$\begin{aligned} \dot{\sigma}_{\text{load}}(\mathbf{r}) = & - \lim_{T \rightarrow \infty} \frac{1}{T} \sum_i \sum_{jk} \left(\left\{ \sum_{n \in S_2^{(i)}(T)} m_{jk}^{(i)(n)}(\mathbf{r}_0) \right. \right. \\ & \times \Psi_{jk}[\mathbf{r}, \mathbf{r}_0, T - t^{(i)(n)}] \Big\} \\ & + \left\{ \sum_{n \in S_1^{(i)}(T)} m_{jk}^{(i)(n)}(\mathbf{r}_0) \Psi_{jk}[\mathbf{r}, \mathbf{r}_0, T - t^{(i)(n)}] \right. \\ & - \sum_{n \in S_2^{(i)}(T)} m_{jk}^{(i)(n)}(\mathbf{r}_0) \Psi_{jk}[\mathbf{r}, \mathbf{r}_0, -t^{(i)(n)}] \Big\} \\ & + \sum_{n \in S_3^{(i)}(T)} m_{jk}^{(i)(n)}(\mathbf{r}_0) \{ \Psi_{jk}[\mathbf{r}, \mathbf{r}_0, T - t^{(i)(n)}] \\ & \left. \left. - \Psi_{jk}[\mathbf{r}, \mathbf{r}_0, -t^{(i)(n)}] \right\} \right) d^2 \mathbf{r}_0. \end{aligned} \quad (6)$$

For large T the second and third terms of equation (6) are negligible, and the Green's function in the first term may be replaced with $\Psi_{jk}(\mathbf{r}, \mathbf{r}_0, \infty)$. This results in

$$\dot{\sigma}_{\text{load}}(\mathbf{r}) = - \sum_i \sum_{jk} \int \langle \dot{m}_{jk}^{(i)}(\mathbf{r}_0) \rangle \Psi_{jk}(\mathbf{r}, \mathbf{r}_0, \infty) d^2 \mathbf{r}_0. \quad (7)$$

The time derivative of moment tensor density in equation (8) is only symbolic and means more precisely

$$\begin{aligned} \langle \dot{m}_{jk}^{(i)}(\mathbf{r}_0) \rangle &= \left\langle \partial_T \sum_{n \in S_2^{(i)}(T)} m_{jk}^{(i)(n)}(\mathbf{r}_0) \right\rangle \\ &= \lim_{T \rightarrow \infty} \frac{1}{T} \sum_{n \in S_2^{(i)}(T)} m_{jk}^{(i)(n)}(\mathbf{r}_0). \end{aligned} \quad (8)$$

The time-averaged moment release rate in equation (8) is proportional to the slip rate on fault i . Equation (7) thus states that the loading rate is that resulting from a prescription of backslip on all faults at their respective long-term slip rates and evaluated on the viscoelastic model in the limit of complete relaxation. This result was previously given in equation (9) of Savage (1983).

In practice, equation (1) is implemented with equations (2), (3), and (7) for the coseismic stress changes, post-seismic stresses, and loading rates, respectively. Thus, the stress may be projected forward from an initial starting time

t_0 with knowledge of the faulting history (in order to evaluate equations 2 and 3) and the mean slip rate on each fault (in order to evaluate equation 7).

The loading rate in equation (4) has been defined such that the time-averaged stressing rate at a given point tends to zero as the time interval becomes arbitrarily large, that is,

$$\lim_{t \rightarrow \infty} \langle \dot{\sigma}(\mathbf{r}, t) \rangle = 0. \quad (9)$$

Pollitz and Schwartz (2008) note that in a complete fault network the system should satisfy equation (9) and be self-driven by its set of faults, that is, without the addition of $\dot{\sigma}_{\text{load}}(\mathbf{r})$. Thus, $\dot{\sigma}_{\text{load}}(\mathbf{r}) = 0$ for a complete fault network. In practice, the group of faults available for analysis is incomplete and $\dot{\sigma}_{\text{load}}(\mathbf{r}) \neq 0$. However, as shown in section 4 of Pollitz and Schwartz (2008), an incomplete fault network can be appended with an auxiliary set of faults such that the resulting $\dot{\sigma}_{\text{load}}(\mathbf{r})$ equals zero while the stress evolution prescribed by equation (1) remains unchanged. Hence, the implementation of equation (1) with the loading rate prescribed by equation (7) is not compromised by the use of an incomplete fault network. The previously described prescription is adequate for time spans that are short enough that the fault network and/or elastic properties themselves do not evolve (e.g., Ben-Zion *et al.*, 1999; Lyakhovsky *et al.*, 2001). We assume that it is adequate for simulations up to several tens of thousands of years.

Earthquake Simulation

Green's Functions

In order to improve the efficiency of evaluating equation (1), it is advantageous to store the Green's functions $\Psi_{jk}(\mathbf{r}, \mathbf{r}_0, t)$ ($t \geq 0$) in computer memory. For the static-deformation component of Ψ_{jk} (i.e., $\Psi_{jk}(\mathbf{r}, \mathbf{r}_0, 0^+)$), the Green's function varies with distance from the source $r = |\mathbf{r} - \mathbf{r}_0|$ as r^{-3} . The postseismic components vary smoothly in the horizontal dimension at shallow depth levels, with dominant wavelength approximately equal to the elastic plate thickness. At depth, however, the postseismic components may vary sharply in the horizontal dimension, with a dominant wavelength roughly equal to the distance of the observation point from the base of the elastic plate. The sharpest horizontal (and vertical) variations in the postseismic component of Ψ_{jk} arise from a source \mathbf{r}_0 close to the base of the elastic layer. This is indicated by the tendency for viscoelastic-mode eigenfunctions to become increasingly concentrated near the base of the elastic layer with increasing spherical harmonic degree (decreasing wavelength), jointly with increasing amplitude (Fig. 2). This occurs fundamentally because the coseismic stress field at the top of the asthenosphere, just below the base of the elastic plate, is large and of short wavelength for a deep source. These stresses must relax with time, and continuity of stress at the elastic plate/asthenosphere boundary dictates that the base of the

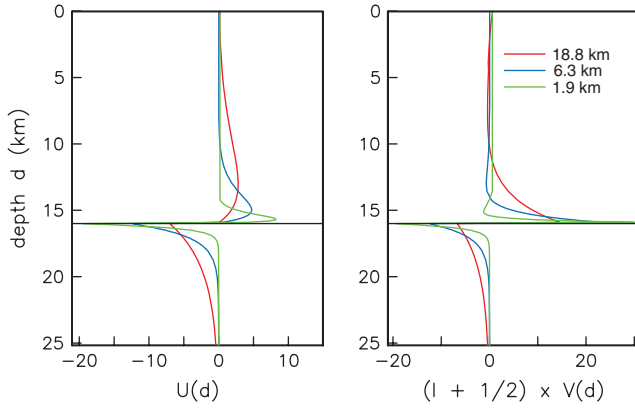


Figure 2. Spheroidal viscoelastic-mode eigenfunctions of the spherically layered viscoelastic model (see Synthetic Stress and Seismicity Patterns), which has an elastic plate thickness of 16 km. Vertical eigenfunction U and horizontal eigenfunction V are shown as a function of wavelength $= 2\pi R/(l + \frac{1}{2})$, where R is Earth's radius and l is the spherical harmonic degree.

elastic layer must have large amplitude with relatively short wavelength. These considerations show that the Green's functions should be discretized relatively densely in the near-source region.

We discretize $\Psi_{jk}(\mathbf{r}, \mathbf{r}_0, t)$ as follows. For a given source \mathbf{r}_0 , define an auxiliary coordinate system with an equator that passes through the surface projection of \mathbf{r}_0 and is parallel to the local east direction at that point. In this coordinate system assign a longitude of zero to \mathbf{r}_0 , and let ϕ and θ be the longitude and latitude of \mathbf{r} .

Assume that each fault patch is of identical length and width, represented by a center point located in the middle of the patch, and that the associated source depth is discretized as

$$d_m = d_{\max} + (d_{\min} - d_{\max})\left(-0.5 + \frac{m}{N_d}\right) \quad (i = 1, \dots, N_d), \quad (10)$$

where N_d is the number of depth points that sample the depth interval from d_{\min} to d_{\max} . The set $\{d_m\}$ also spans the range of receiver depths because we intend to evaluate deformation in the middle of each fault patch.

We define a fundamental source fault patch $\Omega_m^{(\delta)}$ striking due north, with center at depth d_m located at zero latitude and longitude in the auxiliary coordinate system, and with length L , dip δ , and width $W = (d_{\max} - d_{\min})/[(\sin \delta)N_d]$. For the $\alpha\beta$ component of stress in this coordinate system we calculate discrete Green's functions $\Psi_{jk\alpha\beta}^{(\delta)}[(\phi_p, \theta_p, d_p), d_m, t_q]$ for the unit source fault patch, discrete receiver coordinates (ϕ_p, θ_p, d_p) , and discrete times t_q as an integral over the source fault patch:

$$\begin{aligned} & \Psi_{jk\alpha\beta}^{(\delta)}[(\phi_p, \theta_p, d_p), d_m, t_q] \\ &= \int_{\Omega_m^{(\delta)}} \Psi_{jk\alpha\beta}[(\phi_p, \theta_p, d_p), \mathbf{r}_0, t_q] d^2\mathbf{r}_0. \end{aligned} \quad (11)$$

A set of receiver coordinates suitable for this purpose (and used in the present study) is shown in Figure 3. These Green's functions may be computed and stored ahead of time. They embody coseismic and postseismic deformation from prescribed dislocation sources and are calculated using the methods of Pollitz (1996, 1997). Note that in the along strike direction the gridpoints in the near field are spaced exactly one fault length L apart. We may extend the definition of discrete Green's functions by allowing them to be continuous variables of θ and ϕ as well as t , that is

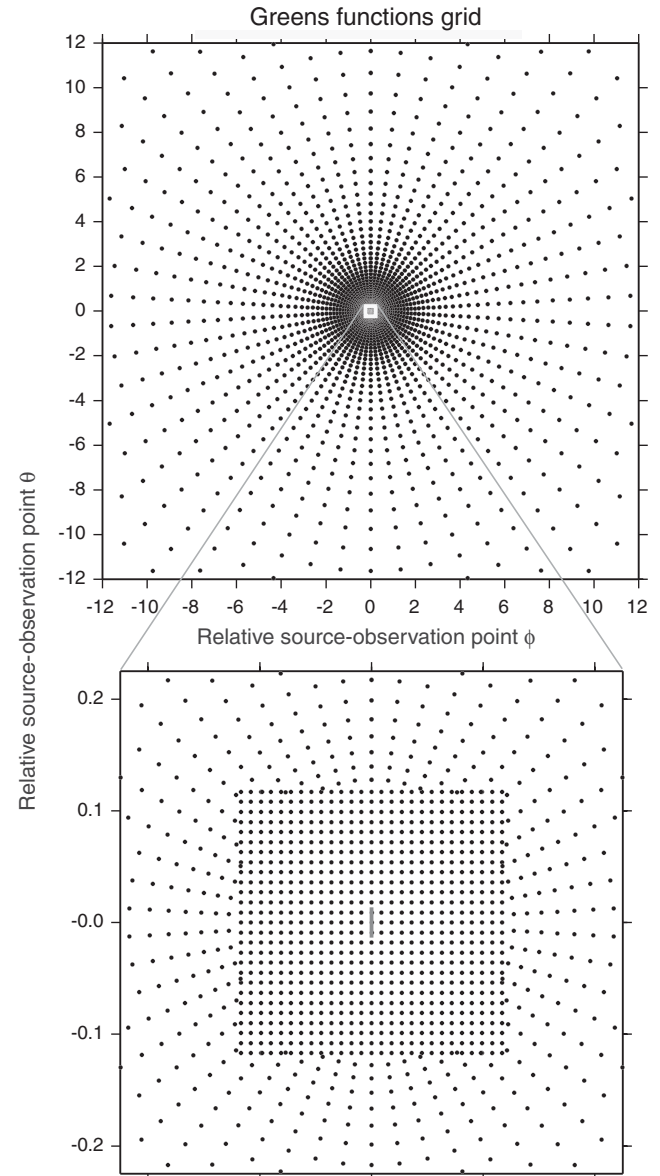


Figure 3. (a) Grid of points used to compute Green's function response for a fundamental source patch. Unit of relative latitude and longitude is degrees. (b) Close-up view of the grid shown in (a). The gray line indicates the surface projection of a 3 km long fundamental source patch, represented by a line parallel to the fault strike and passing through the middle of the source patch.

$\Psi_{jk}^{(\delta)}[(\phi, \theta, d_p), d_m, t]$, which may be obtained through spatial and/or temporal interpolation of the functions given in equation (11).

Calculation of Stress Evolution

Let the physical source fault i have the position $\mathbf{r}_i = (\hat{\mathbf{r}}_i, d_i)$ and strike ψ_i . It is convenient to define the rotated Green's functions

$$\tilde{\Psi}_{jk\alpha\beta}^{(\delta)} = \sum_{\alpha'\beta'} R_{\alpha\alpha'}(-\psi_i) R_{\beta\beta'}(-\psi_i) \Psi_{jk\alpha'\beta'}^{(\delta)}, \quad (12)$$

where $\mathbf{R}(-\psi_i)$ is a rotation matrix that performs a rotation of the given angle about $\hat{\mathbf{r}}_i$ in order to obtain tensor components in the geographic coordinate system. For the stress component $\sigma_{\alpha\beta}$ at observation point $\mathbf{r} = (\hat{\mathbf{r}}, d_p)$, equations (1), (2), (3), (7), and (11) lead to

$$\begin{aligned} \sigma_{\alpha\beta}[(\hat{\mathbf{r}}, d_p), t] &= \sigma_{\alpha\beta}[(\hat{\mathbf{r}}, d_p), t_0] \\ &+ \sum_{jk} \sum_{j'k'} \sum_i R_{jj'}(\psi_i) R_{kk'}(\psi_i) \\ &\times \left(-\langle \dot{m}_{j'k'}^{(i)} \rangle \tilde{\Psi}_{jk\alpha\beta}^{(\delta)}[(\phi, \theta, d_p), d_i, \infty](t - t_0) \right. \\ &+ \sum_{n=1}^{\infty} m_{j'k'}^{(i)(n)} \{ \tilde{\Psi}_{jk\alpha\beta}^{(\delta)}[(\phi, \theta, d_p), d_i, t - t^{(i)(n)}] \\ &\times H[t - t^{(i)(n)}] \}_{|t_0}^t \Big), \end{aligned} \quad (13)$$

where (θ, ϕ) is the running angular distance and azimuth from source point $\hat{\mathbf{r}}_i$ to observation point $\hat{\mathbf{r}}$.

Equation (13) is the main result of Earthquake Simulation. It is used to project stress forward from an initial time t_0 to time t . In practice, time is advanced in increments Δt so that equation (13) is implemented with $t = t_0 + \Delta t$. Then the initial time is reset to $t_0 = t$ and so forth.

For determining stress evolution on the fault network itself, it suffices to evaluate it for points $\hat{\mathbf{r}} = \hat{\mathbf{r}}_p$; however, equation (13) is more general and allows the determination of stress evolution in the regions between faults as well. It is applicable to any stress component or any linear combination of stress components (e.g., the Coulomb failure function).

Computational Efficiency

As time advances new ruptures are generated (see Determination of Earthquake Ruptures), and the faulting history is updated with more events. This means that the n summation in equation (13), which sums over all past events on a given fault, grows with time. Over many earthquake cycles the stress evolution evaluated with equation (13) requires the convolution of a large number of sources with the appropriate Green's functions accounting for the accumulated coseismic and postseismic deformation. This reflects the fact that viscoelastic relaxation retains memory of all past source

loads and continually evolves in response to the past loads. However, the computational burden becomes considerable as past ruptures accumulate with increasing time, so that computational demand in a straightforward application of equation (13) would grow quadratically with elapsed time.

Computational efficiency is gained in three ways:

1. Time-dependent regrouping of past dislocations. If a given patch has ruptured at past times t_1 and $t_2 > t_1$, and the elapsed time since t_2 is much greater than $t_2 - t_1$ (i.e., $t - t_2 \gg t_2 - t_1$), then the viscoelastic relaxation accumulated in the next timestep is nearly insensitive to the time of the slip. That is, the slippage s_1 at time t_1 and slippage s_2 at time t_2 may be combined into a net slip $s_1 + s_2$ at a single time (e.g., either t_1 or t_2). This slip regrouping is assigned to time t_2 if $s_2 > s_1$ and time t_1 if $s_1 \geq s_2$, and it is implemented if $t - t_2 > 7 \times (t_2 - t_1)$. At sufficiently large elapsed times, slip regrouping may involve the same patch multiple times. This procedure ultimately keeps the number of past slip events needed in the n summation bounded.
2. Selective time-sampling of equation (13) and temporal interpolation. It is generally necessary to evaluate equation (13) with the full n summation at least intermittently because of the nonlinearity of the viscoelastic relaxation terms. However, much of the signal from past events varies smoothly with time, and for such events a smooth functional dependence with time may be implemented. However, for very recent events (i.e., small $t - t^{(i)(n)}$ compared with a typical relaxation time) all terms in the n summation must be implemented. This suggests a strategy in which the i and n summations in equation (13) are separated into two groups, one for past events occurring at least a time T in the past and interpolated using a smooth (e.g., quadratic) time dependence, and the other for more recent events, for example,

$$\begin{aligned} \sigma_{\alpha\beta}[(\hat{\mathbf{r}}, d_p), t] &= \sigma_{\alpha\beta}[(\hat{\mathbf{r}}, d_p), t_0] \\ &+ \dots \sum_i \left(\sum_{n|t-t^{(i)(n)} < T} \dots \{ \tilde{\Psi}_{jk\alpha\beta}^{(\delta)}[(\phi, \theta, d_p), d_i, t - t^{(i)(n)}] \times H[t - t^{(i)(n)}] \}_{|t_0}^t \right. \\ &+ \sum_{n|t-t^{(i)(n)} \geq T} \{ A[(\phi, \theta, d_p), d_i, t_0 - t^{(i)(n)}] \times (t - t_0) \\ &\left. + B[(\phi, \theta, d_p), d_i, t_0 - t^{(i)(n)}] \times (t - t_0)^2 \} \right). \end{aligned} \quad (14)$$

The A and B coefficients in equation (14) may be evaluated at a reference time t_0 using equation (13) with the full summation. Then equation (14) may be used to evaluate stress for $t > t_0$ up to a certain time where the quadratic approximation slightly loses accuracy. Tests show that equation (14) is typically very accurate for a choice $T \sim 45$ yr and, starting from an initial t_0 , for times $t_0 < t < t_0 + 15$ yr. Then t_0 may be increased by 15 yr,

new A and B coefficients determined, and so forth. This scheme requires the evaluation of the full n summation in equation (13) only once every 15 yr, during which typically 25 to 50 slip events may occur. The numerical effort involved with evaluating equation (14) is generally an order of magnitude less than that involved with evaluating equation (13), implying a corresponding reduction in computation time.

3. Dynamic timestepping. With knowledge of the stressing rate stored at the current timestep, the time of the next slip event on at least one fault patch in the system may be predicted. The subsequent timestep may be taken just large enough to initiate a new slip event with one evaluation of equation (13) or equation (14).

Determination of Earthquake Ruptures

Ruptures on a set of fault patches initiate, propagate, and terminate according to the evolution of the Coulomb failure function (CFF, King *et al.*, 1994)

$$\text{CFF} = \tau + \mu_{\text{eff}}\sigma_n, \quad (15)$$

where τ and σ_n are shear and normal stress, respectively, resolved onto a fault plane with normal \hat{n} and fixed slip vector \hat{s} , that is, $\tau = \hat{s} \times \sigma \times \hat{n}$ and $\sigma_n = \hat{n} \times \sigma \times \hat{n}$, where σ is the stress tensor; μ_{eff} is the effective coefficient of friction. Referring to Figure 1 we prescribe a cascade mechanism to determine an earthquake rupture. Following Ben-Zion *et al.* (2003), the steps in determining a rupture are as follows:

1. Rupture initiation. Rupture initiates on a fault patch when CFF exceeds a static frictional stress value σ_s . This value may vary from fault to fault.
2. Rupture propagation. At a given timestep, each patch in the fault network is queried. When the stress on one or more fault patch exceeds the static frictional stress threshold, each patch slips the amount necessary to reduce its CFF to the arrest stress level σ_a . During an event, a patch may rerupture if its stress exceeds a dynamic frictional stress value σ_d . Each fault patch slips in isolation, that is, the specified slip amount that is necessary to reduce stress on the given fault patch to σ_a in the absence of other slip events. It is often the case that adjacent fault patches slip simultaneously, in which case each patch immediately reloads the neighboring patches and the resultant stress on any patch is consequently greater than σ_a . During the event (and within the same timestep) the entire fault network is queried once again, and any patches with CFF exceeding its threshold frictional stress will undergo slip events. This may include rupture of new patches or rerupture of patches that already slipped during the current event. Note that an event may include rupture of one or more fault segments (each of which has joined fault patches with smooth transitions, i.e., no large kinks), though the vast majority of events are restricted to one such segment.

3. Rupture termination. Rupture terminates as soon as the fault network is queried and CFF is less than σ_s (or σ_d for patches that have already ruptured) everywhere.

Following Ben-Zion (1996) we assume that the brittle strength follows Byerlee's Law and varies with depth z as

$$\sigma_s = f_s(\rho - \rho_w)gz, \quad (16)$$

where f_s is the static coefficient of friction, ρ and ρ_w are the rock density and water density, respectively, and g is the gravitational acceleration. In equation (16) we shall use values $f_s = 0.75$ and $\rho - \rho_w = 18 \text{ Mpa/km}$ to prescribe the vertical gradient. We assume that $\sigma_a = \sigma_s - \Delta\sigma$, where $\Delta\sigma$ is a constant stress reduction value. Unless specified otherwise, the calculations use $\Delta\sigma = 5 \text{ MPa}$. It is useful to define a dynamic overshoot coefficient $D = (\sigma_s - \sigma_a) / (\sigma_s - \sigma_d)$, which reflects the tendency for the arrest level σ_s to be lower than σ_d . Then $\sigma_d = \sigma_s - D^{-1}(\sigma_s - \sigma_a)$. The system behavior would be unaltered if we were to subtract a reference stress value of $\sigma_s - S$ from the actual stress distribution and adjust the frictional stresses as

$$\sigma_s \rightarrow S \quad \sigma_d \rightarrow S - D^{-1}(\sigma_s - \sigma_a) \quad \sigma_a \rightarrow S - \Delta\sigma. \quad (17)$$

Using S as the reference failure stress threshold simply redefines the stress field relative to the Byerlee frictional strength, and it allows us to visualize stress differences without the depth dependence.

The average stress drop during an event is always less than $\sigma_s - \sigma_a = \Delta\sigma$. A patch will have an instantaneous stress drop of this amount when it is stressed above σ_s , but (except on the patch where the event nucleates) that occurs during an event after the stress on the patch has been increased by stress transfer from neighboring patches. As a corollary the stress drop is generally not constant on the fault, even when $D = 1$, because the stress state just before an event is generally heterogeneous. The only definite statement that can be made in this regard is that the stress drop on patches that slip in an event must be between $\sigma - \sigma_a$ and $\sigma - \sigma_d$, where σ is the preevent stress; the stress drop equals $\sigma - \sigma_d$ when $D = 1$.

In the fault networks employed in this article, stresses are evaluated in the center of patches of dimension 3 km (in length) \times 2 km (in depth). The amount of slip needed to reduce the stress of a patch by 5 Mpa is 40 cm, implying that the minimum earthquake magnitude is 5.2.

Stress and Seismicity Functions

We employ several measures to characterize stress evolution on system faults. These stress functions are among those given in section 2.2 of Ben-Zion *et al.* (2003).

1. Average stress,

$$AS(t) = \frac{1}{N} \sum_{i=1}^N \tau_i(t), \quad (18)$$

where τ_i is a stress value at time t (e.g., CFF) and patch i on a fault with N patches. AS is expected to be relatively high/low just before/after a large event.

2. Standard deviation of stress,

$$SD(t) = \sqrt{\frac{1}{N} \sum_{i=1}^N [\tau_i(t) - AS(t)]^2}. \quad (19)$$

This measures the size of stress fluctuations on the fault, with large values of SD indicating a more heterogeneous distribution of stress on the fault.

3. Configurational entropy,

$$CE(t) = - \int p[s(t)] \ln\{p[s(t)]\} ds, \quad (20)$$

where $p[s(t)]$ is the density distribution of stress on a given fault at time t (note that $\int p[s(t)] ds = 1$). This measure characterizes the evolving number of stress states on the fault, a larger value of CE indicating a greater number of stress states and higher degree of disorder.

We employ the following functions of seismicity:

1. We compile histograms of the interevent times for events about a threshold magnitude on a given fault. This uses the entire history of simulated seismicity.
2. We track the cumulative number of slip episodes up to time t on fault patches (belonging to a given fault) within a definite depth range. A related function is the cumulative amount of slip within a definite depth range averaged over the length of the given fault.
3. A foreshock–mainshock (FM) triggering measure $FM(M, T)$, the probability that a moderate magnitude event will be followed with a time T by an event of magnitude $> M$. Moderate events of magnitude between 5.9 and 6.2 are used for this purpose. This uses the entire history of simulated seismicity.
4. The frequency (f) versus magnitude statistic is calculated using the entire history of simulated seismicity.

Application to Synthetic Fault Network

Fault Geometry and Viscoelastic Structure

We define a synthetic fault network consisting of two parallel, vertical, strike-slip faults, each extending from the surface to the base of the elastic plate at 16 km depth (Figs. 4 and 5). Each fault is 300 km long, and they are separated by 32 km. Each fault is discretized into 3×2 km (length times depth, respectively) patches, resulting in 800 patches per fault.

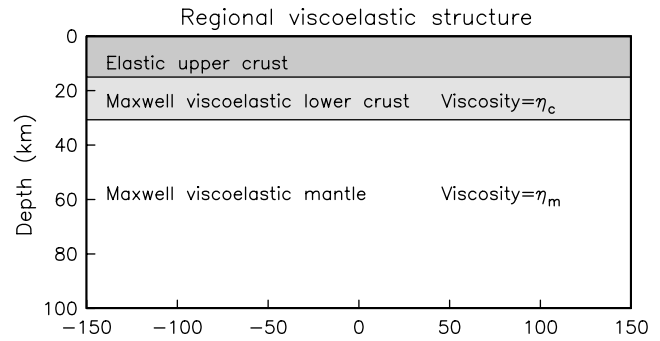


Figure 4. Viscoelastic stratification used in this study, consisting of an elastic upper crust underlain by Maxwell viscoelastic lower crust of viscosity η_c and mantle of viscosity η_m .

Each fault is assigned a simple slip history, which drives the initial viscoelastic relaxation of the system. Fault 1 had a 3 m uniform slip in the year 1900, and fault 2 had a 1.5 m uniform slip in the year 1900. The viscoelastic structure consists of a 16 km thick elastic upper crust underlain by a Maxwell viscoelastic lower crust and mantle. Uniform elastic parameters are assigned to the upper and lower crust: shear modulus $\mu = 30$ GPa and bulk modulus $\kappa = 50$ GPa. The mantle is assigned elastic parameters $\mu = 70$ GPa and $\kappa = 117$ GPa. Following Pollitz and Nyst (2004), the viscosity values are $\eta_c = 4.0 \times 10^{19}$ Pa s and $\eta_m = 1.2 \times 10^{19}$ Pa s.

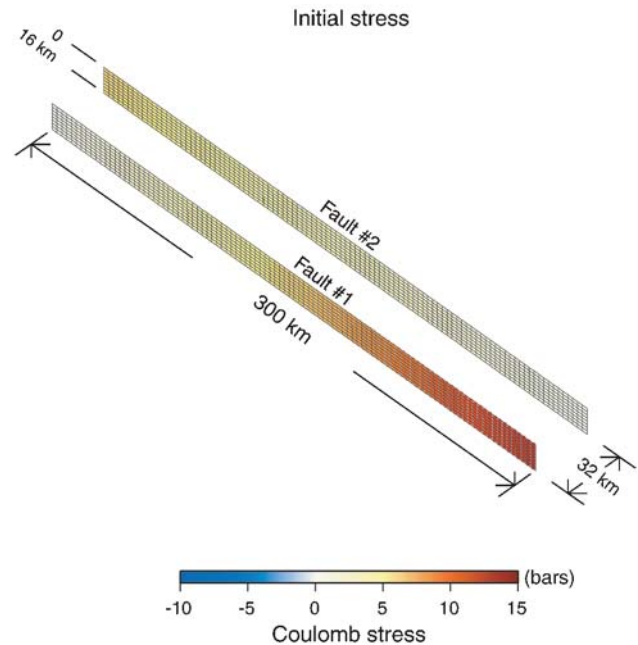


Figure 5. Synthetic fault network, consisting of two 300 km long, 16 km wide vertical right-lateral strike-slip faults separated by 32 km. Each fault is discretized into 800 patches with dimensions of 3×2 km. The assigned initial stress field is superimposed.

Implications of Viscoelasticity

With reference to the pre-1900 stress field, Figure 6 shows the contribution of fault 1 to the subsequent stress evolution. The figure shows right-lateral shear stress at the time of the coseismic offset and for three postseismic epochs; the stresses correspond to the terms $[\sigma_{co}^{(i)}(\mathbf{r}, t)|_{t_0}]$ and $[\sigma_{ps}^{(i)}(\mathbf{r}, t)|_{t_0}]$ of equation (1). The largest coseismic stress drops are on the lower edge and lateral ends of the faults, as expected. Postseismic stress changes are positive everywhere, corresponding to reloading of the fault zone, and they are largest at the base of the fault. Thus, the postseismic stress changes exhibit the same pattern as the coseismic stress change and with opposite sign. With sufficient elapsed time, it is found that the accumulated postseismic stress changes nearly negate the coseismic stress change. For an infinitely long strike-slip fault in a one-fault system, the summed coseismic and postseismic stress changes in the limit of complete relaxation would be theoretically zero (Savage and Prescott, 1978; Pollitz, 2001), because the resultant motion would simply be block motion of one side of the fault with respect to the other. From equation (7) this implies that $\dot{\sigma}_{load}$ is zero for an infinitely long strike-slip fault and nearly zero for a finite length fault.

This reasoning carries an unexpected implication. $\dot{\sigma}_{load}$ is zero if the defined fault network is kinematically self-consistent (Pollitz and Schwartz, 2008), that is, it contains a prescription of faults and slip rates such that the long-term motion of the volumes between the faults is rigid (as would be the case for an infinitely long strike-slip fault or several such faults parallel to one another). Because a priori slip rates appear explicitly in the model only through $\dot{\sigma}_{load}$ via the time-averaged moment release rate on a fault, a system with $\dot{\sigma}_{load} = 0$ implies an inherent ambiguity of subsequent stress evolution because all information concerning these slip rates is absent. Put another way, in a kinematically self-consistent model the stress evolution is driven only by viscoelastic relaxation from past earthquakes as in the model of Savage and Prescott (1978). If the past earthquake history on a given fault contains mostly events of the expected size and frequency but also a few anomalously large events in the recent past, then one can imagine that the system will load itself more rapidly and continue to produce such events at a high rate, so that the fault may not have the same average slip rate in the future as it had in the past. Conversely, a fault may spiral to a state of very little average slip rate if because of the circumstances of the stress evolution, it has a few recent smaller than expected events and hence starts to reload less rapidly. This situation in the viscoelastic realm implies that average slip rates on the faults will depend chiefly on the parameters of the cascade model (Determination of Earthquake Ruptures) and partly on the earthquake history prior to initiation of the model.

In the conventional backslip model (Savage, 1983) the net loading rate on a fault (even an infinitely long fault) does depend explicitly on a priori slip rates. Because the conventional backslip model is an end-member case of viscoelasticity

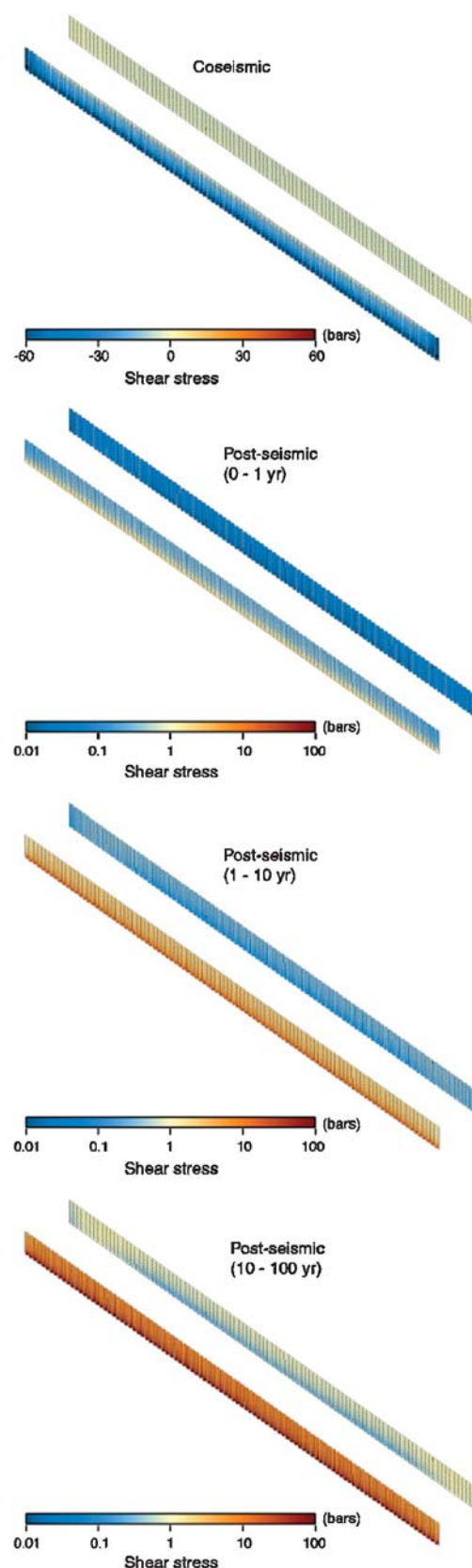


Figure 6. Evolution of right-lateral shear-stress resulting from 3.0 m of slip on fault 1 in the viscoelastic model. Coseismic stress change is plotted on a linear scale, postseismic stress changes are plotted on a logarithmic scale.

city in the limit of large asthenosphere viscosity (Savage and Prescott, 1978; Savage, 2000; Pollitz, 2001), the absence of explicit dependence on a priori slip rate for the finite viscosity case seems paradoxical. The explanation lies in the fact that the fault is loaded by a sum of viscoelastic relaxation from an infinite number of past earthquakes, for example, the $\sum_i [\sigma_{ps}^{(i)}(\mathbf{r}, t) |_{t_0}^{t_i}]$ term of equation (1). In the high viscosity limit the recent earthquake history is immaterial because the viscoelastic relaxation from a finite number of past events tends to zero with large viscosity. Because the past earthquake history is assumed to consist of slip events that, on average, obey the a priori slip rate, the resultant viscoelastic relaxation from past earthquakes is proportional to the a priori slip rate. In the finite viscosity case, the dependence on a priori slip rate is compromised by the dependence on recent earthquake history.

The synthetic fault network considered here does, in fact, retain an explicit dependence on slip rate because the process of backslip on the completely relaxed model, used to calculate $\dot{\sigma}_{load}$, is equivalent to specifying additional infinitely long faults off the ends of the model faults, slipping steadily at long-term slip rates prescribed for the respective faults. (In a spherical geometry, the additional faults would be small circles connecting the endpoints of a given fault.) Thus, a priori slip rates communicate with the rest of the model through the interaction of the additional creeping faults with the endpoints of the model faults.

Synthetic Stress and Seismicity Patterns

The long-term slip rates assigned to faults 1 and 2 are 15 mm/yr and 7.5 mm/yr, respectively. In order to approximate a transition to slip-strengthening behavior in the mid-crust, the fault patches at the bottom of the elastic layer (i.e., 14–16 km depth) release 75% of this slip seismically and 25% aseismically; this is implemented implicitly with equation (7) by assigning a value of mean moment release rate $\langle \dot{m}_{jk}^{(i)}(\mathbf{r}_0) \rangle$ in the 14–16 km depth range that is 75% of its value elsewhere. An initial right-lateral shear-stress distribution in the year 2000 is defined on the faults (Fig. 5) such that the corresponding CFF on fault 1 increases linearly with along strike distance from zero at its northern end to a maximum of 12 bars at its southern end, and CFF on fault 2 increases linearly with distance from zero at its southern end to a maximum of 6 bars at its northern end. We use frictional stress values given in Determination of Earthquake Ruptures with a dynamic overshoot coefficient $D = 1.5$. Simulations are run up to a maximum of 50,000 events or 50,000 yr elapsed time, whichever occurs first.

Beginning in the year 2000, relaxation from pre-2000 events (i.e., the events specified to have occurred in 1900) modifies the initial stress level according to equation (13), which is carried forward in time in increments $\Delta t = 0.1$ yr. Initial earthquake rates are elevated because of the initial conditions, which lead to a first large event rupturing fault 1 in 2004 with M_w 7.8 and a first large event rupturing

fault 2 in 2023 with M_w 7.7. Up to 3 m slip is involved in these first events, which produce an early phase of relatively fast viscoelastic relaxation and hence elevated loading rates. The earthquake sizes and reloading rates stabilize after ~ 400 yr. Figure 7 shows the slip distributions of 12 consecutive $M_w > 6.7$ events occurring after 2400. Typical maximum slip is about 1.8 m, occurring at intervals of ~ 120 yr on fault 1 and ~ 240 yr on fault 2; this is consistent with their respective a priori maximum slip rates.

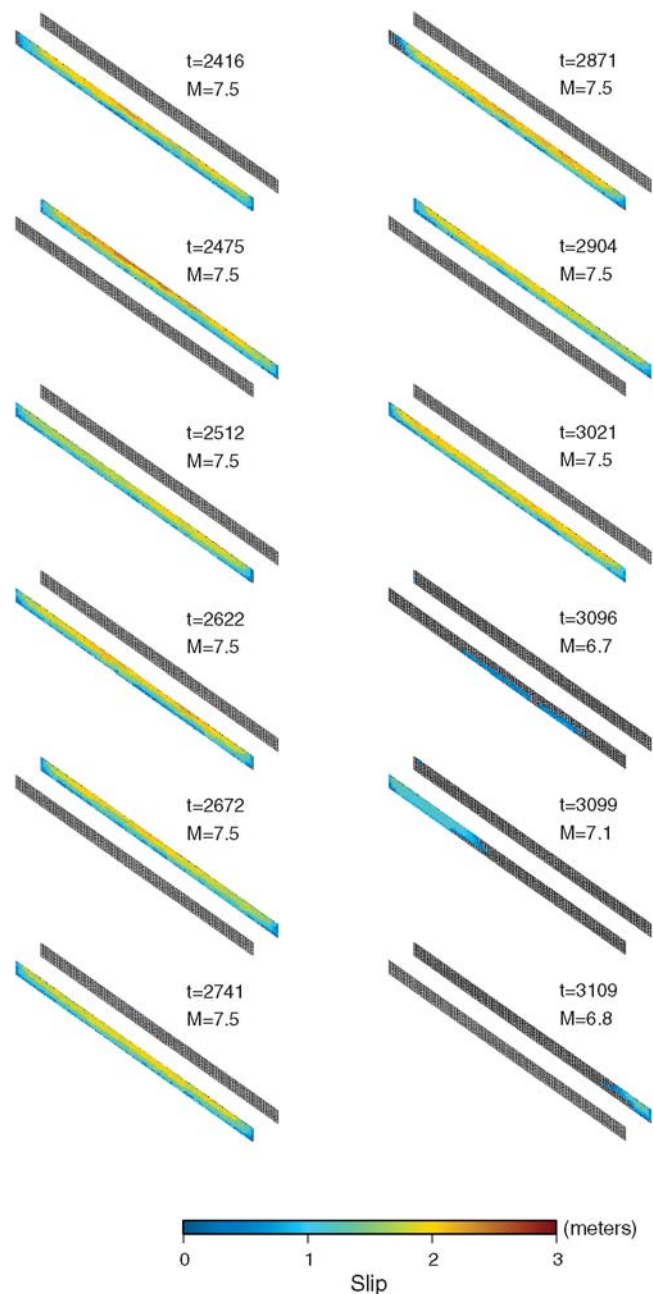


Figure 7. Slip distributions of 12 consecutive $M_w > 6.7$ events occurring in the two-plane model more than 400 yr after initiation of the system. The year and magnitude are noted next to each slip distribution.

The depth-dependence of slip is revealed in Figure 8, which shows average time-dependent slip within several depth intervals on the two model faults. The shallower the depth level, the more episodic the slip. Within the upper 2 km, most slip occurs in $M > 7$ events, whereas at depth $\gtrsim 12$ km, slip occurs more frequently in relatively small magnitude events (Fig. 9). This reflects the overall greater net loading rate as the base of the elastic layer is approached, which arises from the greater magnitude of postearthquake stressing rate contributed by viscoelastic relaxation at greater depth levels. The slip history indicated by the 1000 yr time frame in Figure 8 is consistent with a seismic slip release rate of 15 mm/yr and 7.5 mm/yr on faults 1 and 2, respectively, within 0–12 km; the seismic slip release rates are 25% smaller within the 14–16 km depth interval because 25% of the long-term slip is accommodated by aseismic slip.

On both faults, configurational entropy, average stress, and standard deviation in stress tend to increase with time, leading up to a major ($M \sim 7.5$) rupture (Fig. 10), and all drop suddenly at the time of the earthquake. This behavior is similar to that obtained by Ben-Zion *et al.* (2003) in their model F, who interpret this pattern as an increase in disorder during the buildup period to a system-sized event. During that time numerous small events occur, increasing the number of stress states and the overall level of heterogeneity on the fault. The magnitude-frequency statistics (Fig. 11) illustrate a linear trend up to a magnitude of ~ 7.0 , beyond which the number of events reaches a local maximum at higher frequency than the linear trend. This behavior is commonly

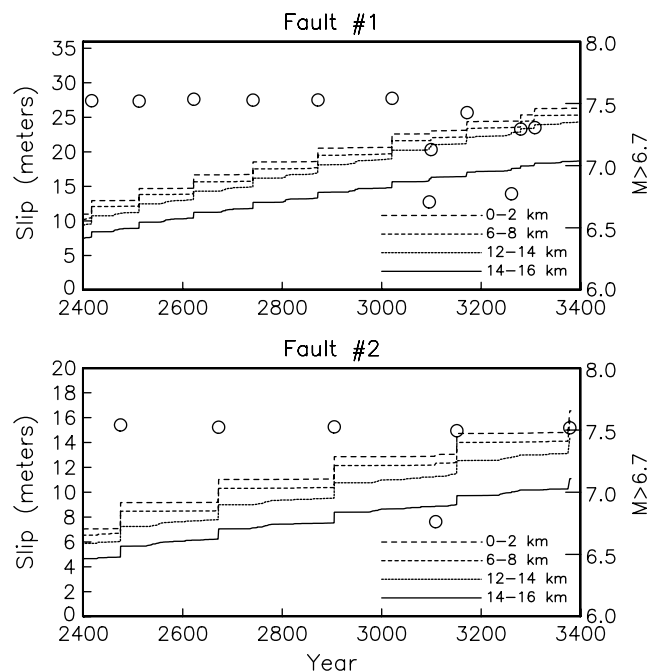


Figure 8. Cumulative average time-dependent slip within indicated depth intervals along faults 1 and 2. Cumulative slip values are zero at the initial time 2000. Superimposed are the times and magnitudes of $M > 6.7$ earthquakes on the respective faults.

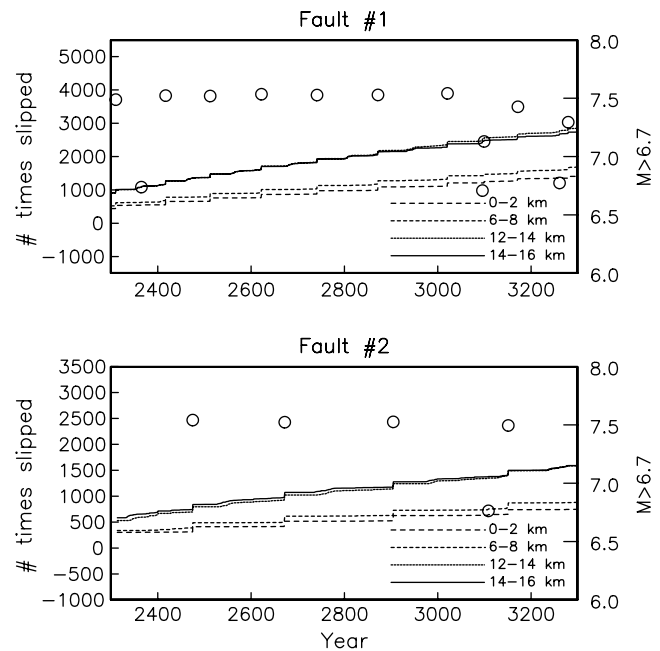


Figure 9. Cumulative number of slip episodes within indicated depth intervals along faults 1 and 2. Superimposed are the times and magnitudes of $M > 6.7$ earthquakes on the respective faults.

seen in synthetic seismicity simulations involving long smooth faults with uniform frictional properties (e.g., Ben-Zion and Rice, 1997; Shaw and Rice, 2000). It is consistent with combined Gutenberg–Richter and characteristic earthquake behavior (Wesnousky, 1994).

Interevent times for $M > 7.3$ events on the model faults are centered on roughly 115 yr for fault 1 and 230 yr for fault 2 (Fig. 12a). Both the interevent times and COV are more variable on fault 1 as D and η_m are varied. The only intrinsic difference between the two faults is the fact that fault 1 has a greater slip rate and ruptures more often than fault 2. It receives quasiperiodic stress perturbations from fault 2 roughly once every two fault 1 cycles. On the other hand, fault 2 receives quasiperiodic stress perturbations from fault 1 roughly twice every fault 2 cycle. To consider an end-member case, assume that large earthquake occurrence is almost perfectly regular on both faults. On fault 1 there is generally equal likelihood of zero or one perturbations from a large fault 2 event during a fault 1 cycle, and on fault 2 it is almost certain that there will be exactly two perturbations from a large fault 1 event during a fault 2 cycle. This qualitative argument suggests that fault 1 is more sensitive to external perturbations than fault 2 because of its larger slip rate, other factors (e.g., fault length) being equal.

The probability of a foreshock–mainshock sequence on each fault is summarized in Figure 13a. For example, with $T = 14$ yr (maximum delay) between a moderate earthquake and a mainshock, the probability of such a sequence is greater than 10% for mainshock magnitudes of 7.3 or less on fault 1. On fault 2, the probability of such a sequence is about

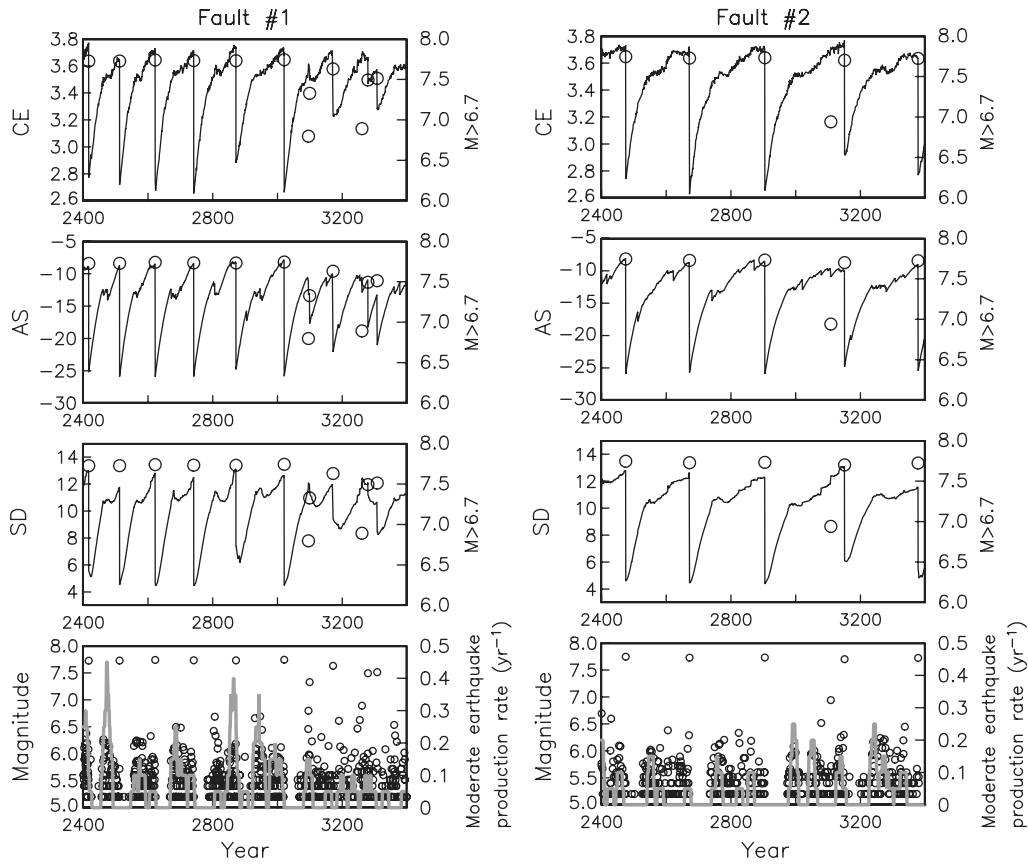


Figure 10. Configurational entropy, average stress, and standard deviation in stress as a function of time. For each fault, the lower plot shows the time and magnitude of all model earthquakes within this time period. Moderate earthquake production rate is calculated using the magnitude range $5.9 < M < 6.2$.

one-half that of fault 1 for all considered mainshock parameter values. This difference reflects the generally longer interevent time between large ruptures on fault 2. The Poissonian probability of a mainshock occurring within this time period by chance is

$$p = 1 - \exp(-ft), \quad (21)$$

where $t = 14$ yr. For a mainshock magnitude threshold of $M 7.3$, the obtained p is generally 20% to 30% greater than the Poissonian value for both faults. For example, taking the case $D = 1.5$ and $\eta_m = 1.2 \times 10^{19}$ Pa s, at this magnitude threshold fault 1 has an 11% probability of experiencing a mainshock within 14 yr of a moderate earthquake. The probability of an $M > 7.3$ mainshock occurring within this time period by chance is given by equation (21) with $f = 6.03 \times 10^{-3} \text{ yr}^{-1}$ based on Figure 11, yielding 8.1%. The same calculations for fault 2 yield a 7.5% probability of experiencing an $M > 7.3$ mainshock within 14 yr of a moderate earthquake, compared with a 5.1% Poissonian probability.

These results and the correlation with the stress measures suggest that moderate earthquakes are diagnostic of special conditions that exist on the fault prior to a mainshock. To determine the significance of this in the context of main-

shock triggering, it would be necessary in future work to investigate whether the moderate events themselves tend to trigger the subsequent mainshock. This would provide a test of the idea that foreshock–mainshock and mainshock–aftershock triggering mechanisms are essentially the same (Feltzer *et al.*, 2004), both being consistent with a static cascade model.

Similar modifications in rupture probability apply when the adjacent fault has just ruptured in a large event, delaying the occurrence of the next large event. This is illustrated in Figure 14, which shows the probability of an $M > 7.3$ event on fault 1 or fault 2 within a certain time interval following an $M > 7.3$ event on the other fault. Rupture probabilities are substantially reduced relative to the Poisson probabilities for several decades following a large event on the adjacent fault. The stress shadow effect is only temporary because large events on the adjacent fault are built into the Poissonian probabilities and the average rupture probabilities over very long time spans (hundreds of years) are the same for the Poissonian (dashed curves) and time-dependent (continuous curves) cases. Thus, an initial relative reduction in rupture probability must be matched by a relative increase in rupture probability after sufficient elapsed time.

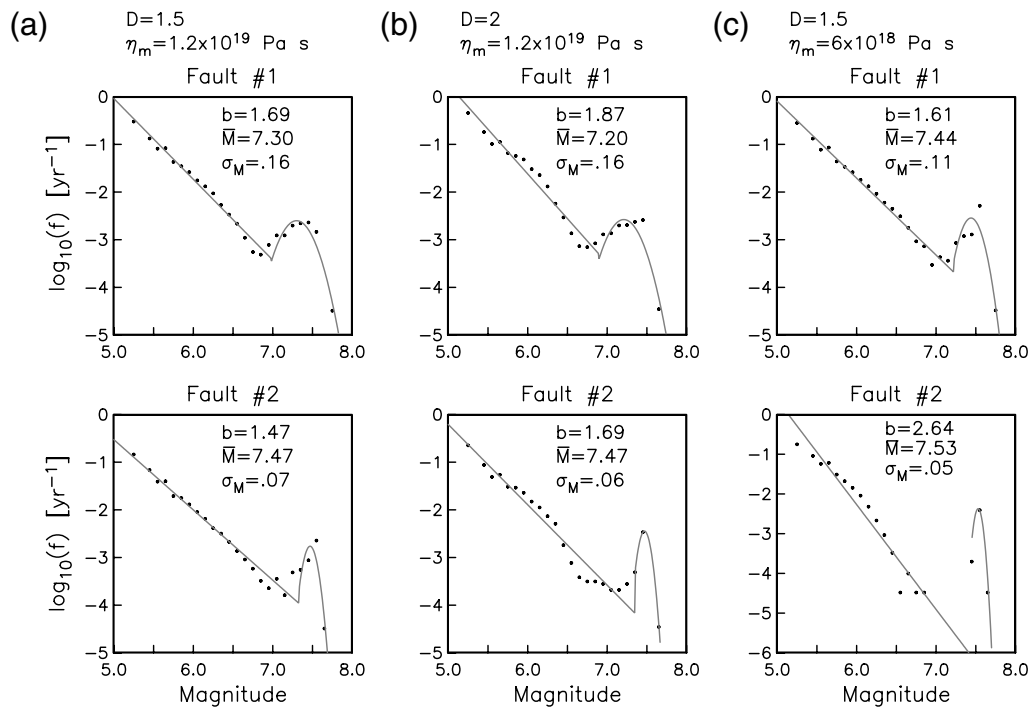


Figure 11. Frequency of earthquake occurrence on each fault of the two-fault model as a function of D and η_m . Event frequency is compiled in bins of 0.1 magnitude unit. Superimposed for each distribution is the best-fitting curve given by equation (22). Best-fitting parameters $\{b, \bar{M}, \sigma_M\}$ are indicated.

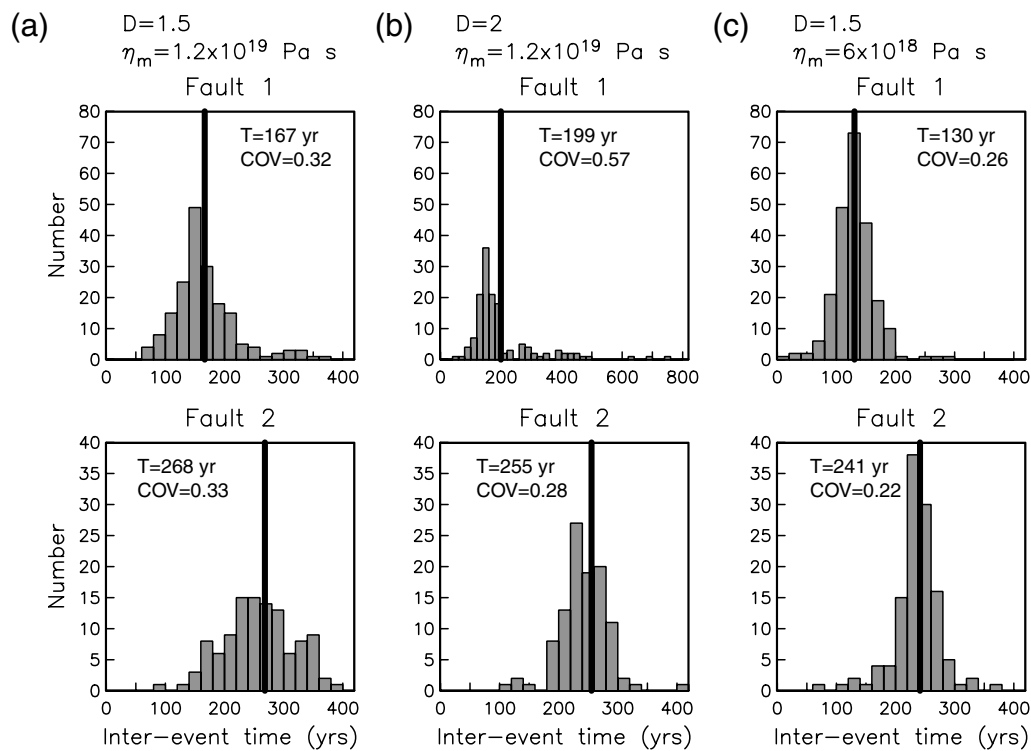


Figure 12. Histograms of interevent times of $M > 7.3$ events on the model faults as a function of D and η_m . The histograms are binned in 20 yr time intervals. Mean recurrence interval (vertical black line segments) and coefficient of variation values are indicated.

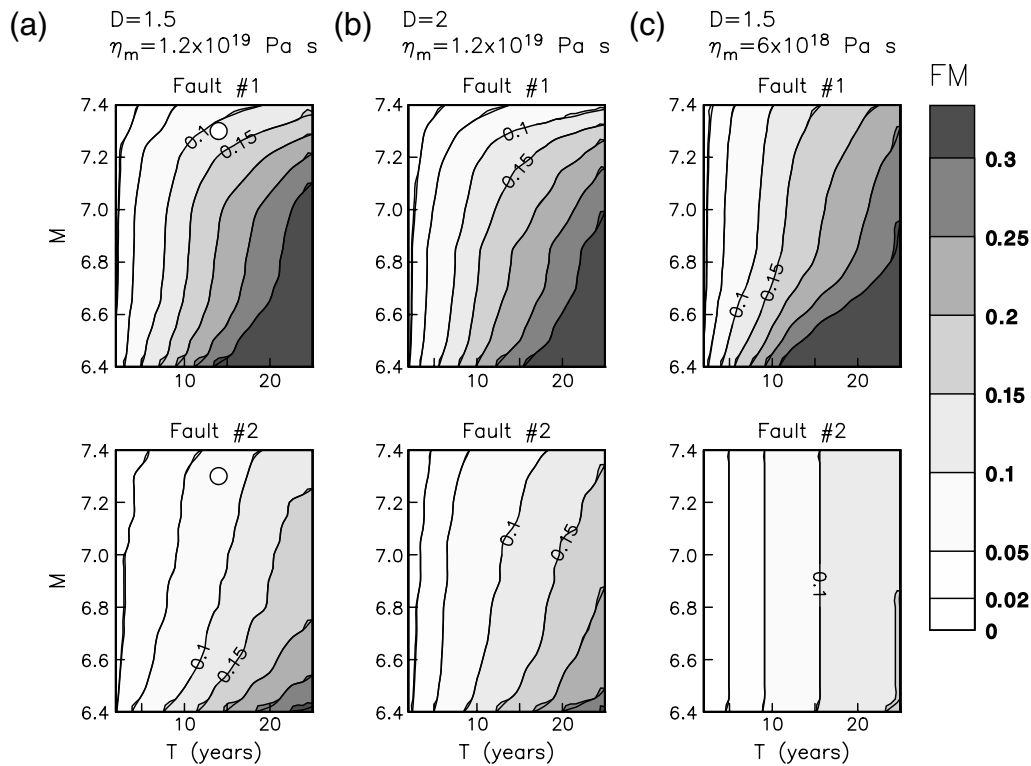


Figure 13. The foreshock-mainshock function $FM(M, T)$: the probability of a (potential) foreshock of magnitude between 5.9 and 6.2 triggering a mainshock of magnitude $\geq M$ within a time period T . The function is evaluated on each fault separately as a function of D and η_m .

Application to San Francisco Bay Region

We exploit an available fault-rupture chronology and fault network assembled by Pollitz and Schwartz (2008) for the purpose of evaluating future stress evolution in the San Francisco Bay region (SFBR). We utilize these same elements to construct a synthetic fault network and an initial stress field, with the capability of projecting the stress field forward in time on a viscoelastic Earth model.

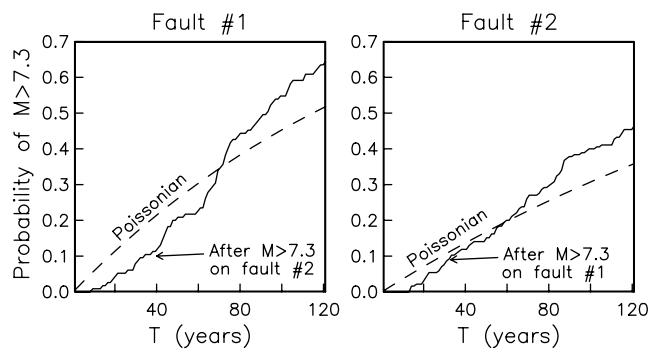


Figure 14. Continuous curves show the probability of an $M > 7.3$ event on fault 1 or fault 2 within a time T following an $M > 7.3$ event on the other fault. Dashed curves show the corresponding Poissonian probability of an $M > 7.3$ event within a time span of T yr. Parameter values are $D = 1.5$ and $\eta_m = 1.2 \times 10^{19}$ Pa s.

Fault Geometry

A discretized fault network consisting of SFBR faults is shown in Figure 15. It is discretized into 2319 patches of faults of uniform length (3 km) and uniform distance (2 km) between the upper and lower edge depths. Most faults extend from the surface to a depth of 16 km, which is also the prescribed elastic plate thickness in the viscoelastic model (Fig. 4); some faults, such as those associated with the 1989 Loma Prieta earthquake, do not rupture up to the surface. Most faults are vertical and accommodate strike slip;

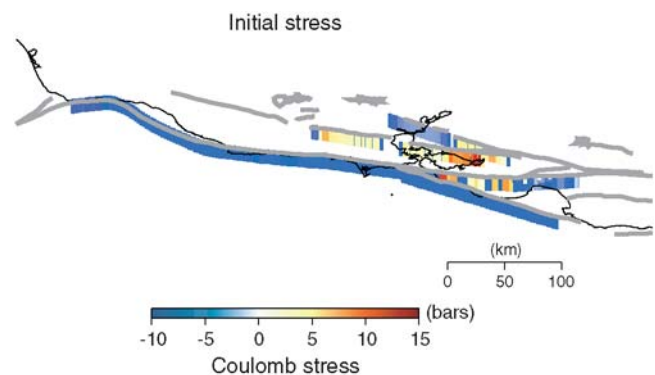


Figure 15. Synthetic fault network in the SFBR. The assigned initial stress field is superimposed. Thick gray lines delineate several major area faults.

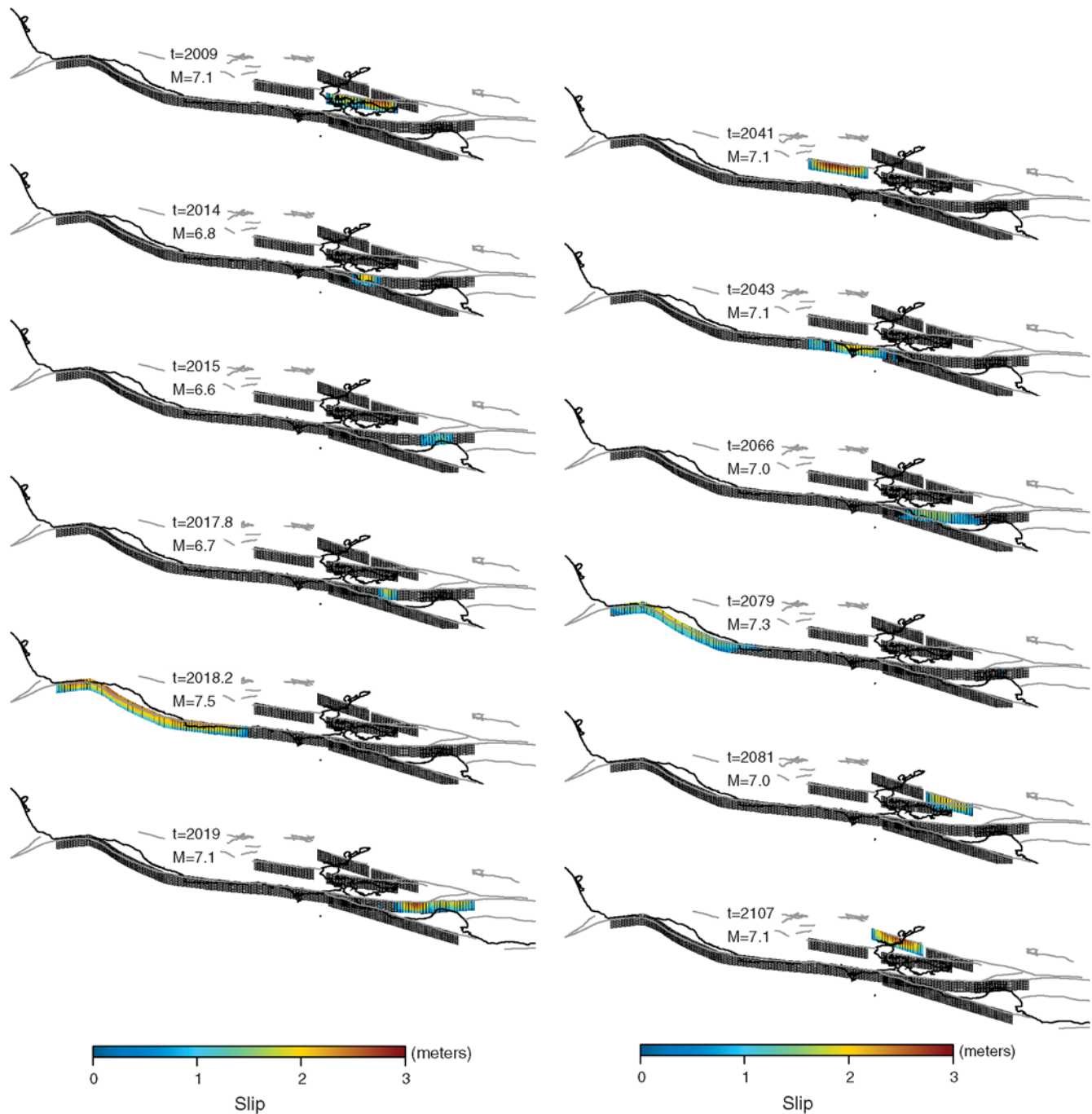


Figure 16. Slip distributions of 12 consecutive $M_w > 6.5$ events occurring in the SFBR model just after initiation of the system. The year and magnitude are noted next to each slip distribution. Parameter values are $D = 1.5$ and $\eta_m = 1.2 \times 10^{19}$ Pa s.

only the fault associated with the 1989 Loma Prieta earthquake is dipping and accommodates dip slip.

The fault network encompasses most major faults of the SFBR. This includes the San Andreas fault, which ruptured most recently in 1906, and the Hayward fault, which ruptured most recently in 1868. Except for the source region of the 1989 Loma Prieta earthquake, all other faults last had major ruptures at least two centuries ago. Parameters associated with fault geometry and fault history are given in ta-

bles 1–3 of Pollitz and Schwartz (2008). The past earthquake history and the long-term slip rates prescribed in that study suffice to project stress forward in time using equation (1) provided that an initial stress field, representative of the present-day stress field, is prescribed.

Initial Stress Field

A guide to the present-day stress field is provided by the SFBR stress evolution model of Pollitz and Schwartz (2008).

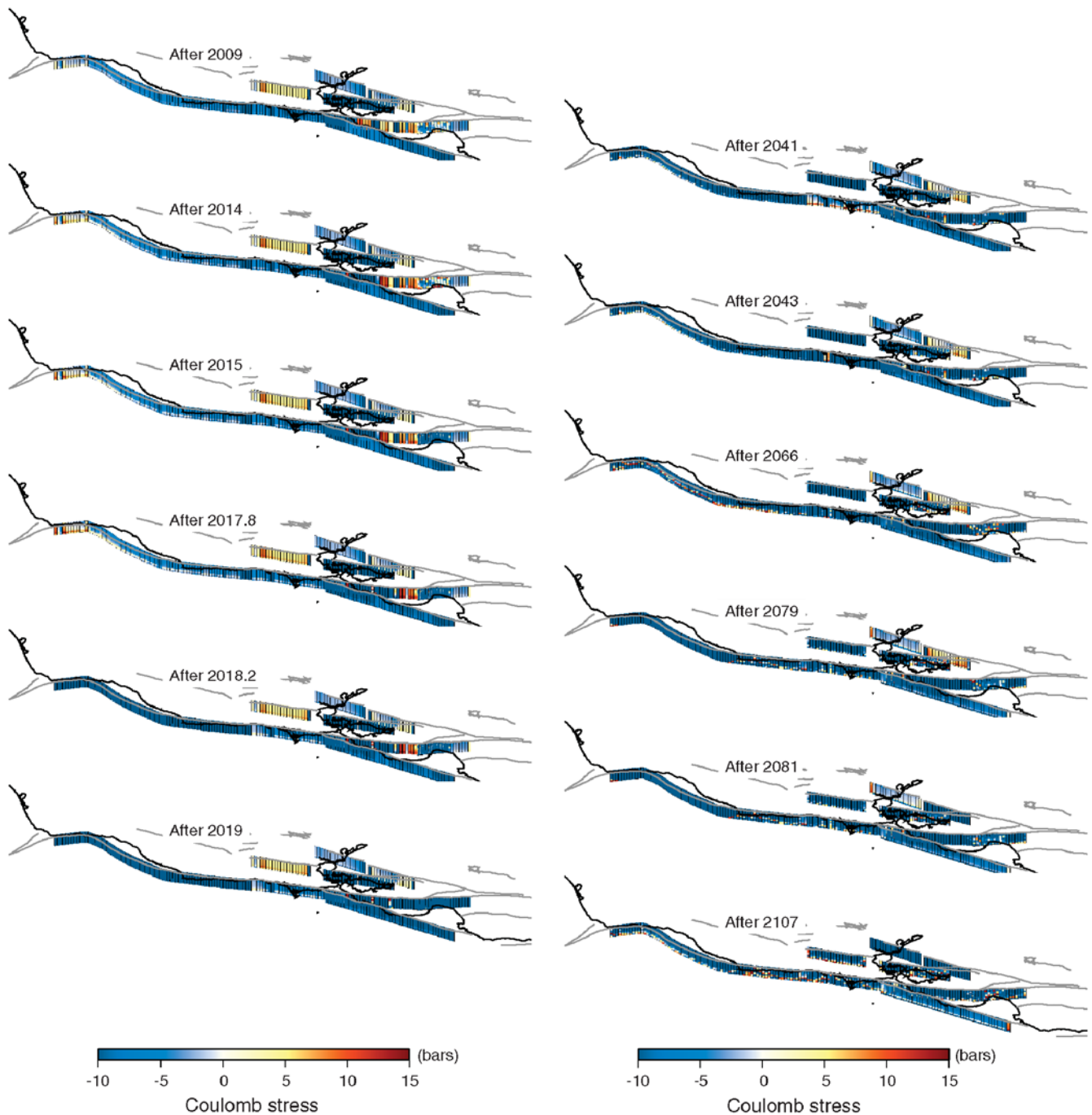


Figure 17. CFF on the fault network following each of six consecutive $M_w > 6.5$ events occurring in the SFBR model (Fig. 17).

Assuming a null stress field at an arbitrary starting time of 1656 (250 yr before the 1906 earthquake), they used equation (1) combined with the assumptions of uniform recurrence intervals and uniform slip per event to evaluate regional stress for the past 350 yr. We adopt their resulting stress field, evaluated at 8 km depth in the year 2000 and with the following caveats, as the initial stress field in the present study. The computations of postseismic relaxation fields in Pollitz and Schwartz (2008) were based on a set of viscoelastic normal modes truncated at relatively long wavelength.

The employed mode set was adequate for the evaluation of postseismic deformation at 8 km depth but not at depths near the base of the elastic plate. We simplify our task by extrapolating the stress field determined at 8 km to patches at all depths, that is, each 3 km long set of patches (16 wide for a vertical fault) is assigned the same initial stress value. The resulting initial stress field is shown in Figure 15. Because the deeper parts of faults undergo relatively large stress fluctuations during a seismic cycle, it is unlikely that the deeper parts share the same stress field as the shallower parts. The

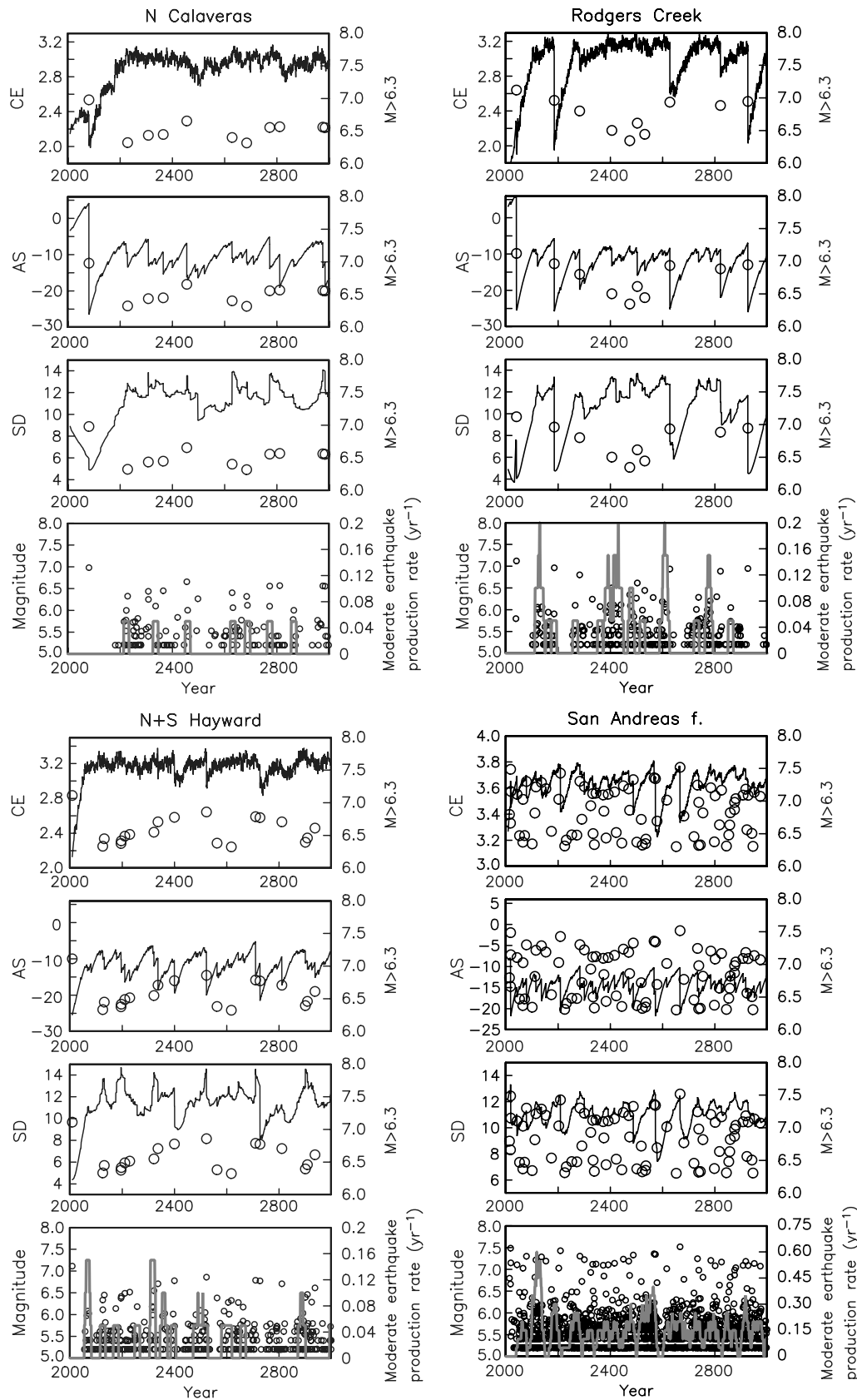


Figure 18. Configurational entropy, average stress, and standard deviation in stress as a function of time for four of the SFBR faults using $D = 1.5$ and $\eta_m = 1.2 \times 10^{19}$ Pa.s. For each fault, the lower plot shows the time and magnitude of all model earthquakes within this time period. Moderate earthquake production rate is calculated using the magnitude range $5.9 < M < 6.2$.

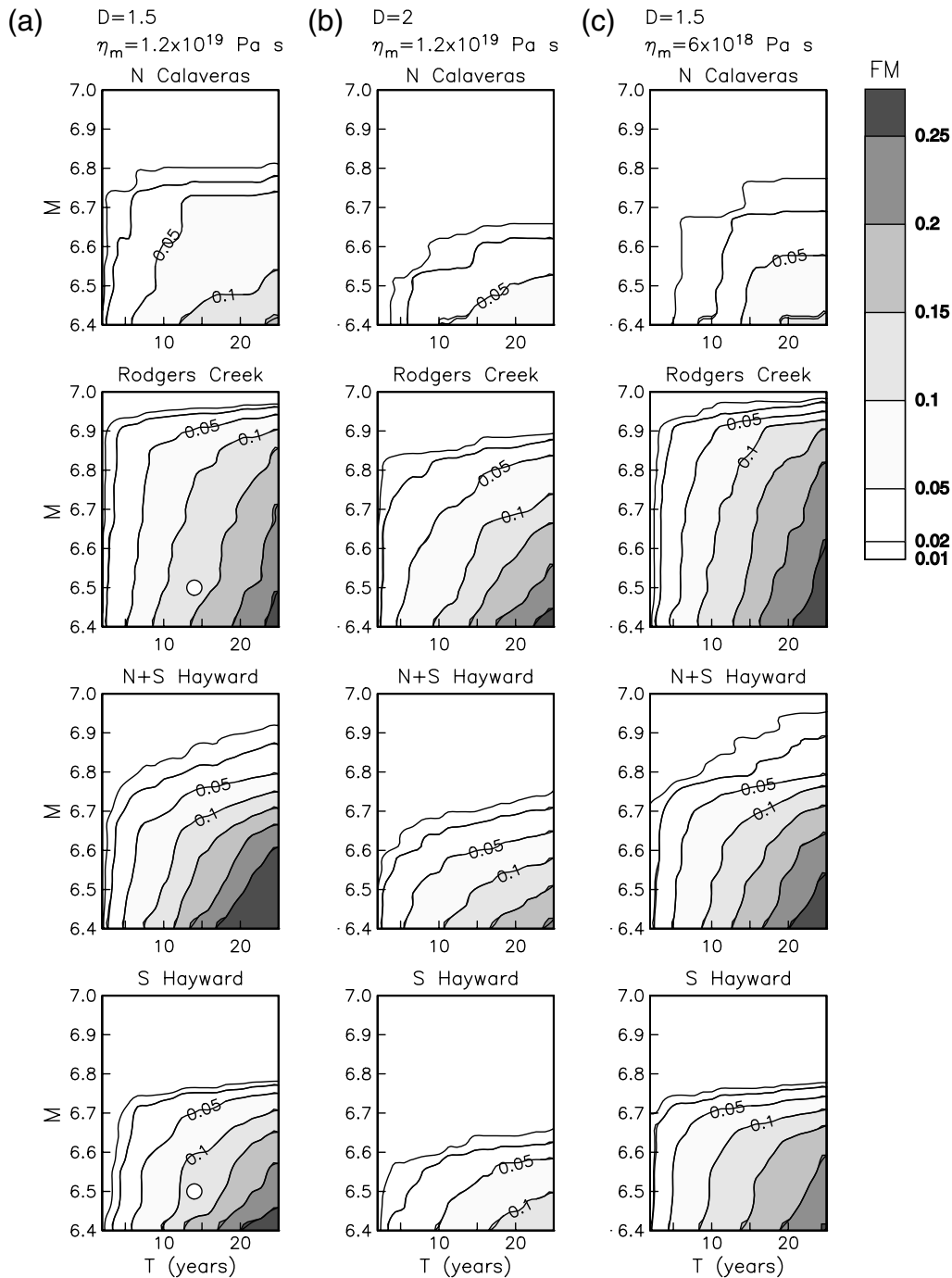


Figure 19. The foreshock–mainshock function $FM(M, T)$: the probability of a (potential) foreshock of magnitude between 5.9 and 6.2 triggering a mainshock of magnitude $\geq M$ within a time period T . The function is evaluated on each of four SFBR faults separately as a function of D and η_m . White circles indicate $M=6.5$ threshold at $T=14$ yr for two of the faults.

number of faulting cycles implemented on SFBR faults was relatively few (generally only one to three past ruptures per fault segment). This means, in effect, that the balance between stress accumulation and stress release expected in the long term (e.g., equation 9) has not been fully achieved during only a 350 yr period of faulting. All of the factors just discussed contribute considerable uncertainty to the initial stress field.

Future Fault Evolution

The SFBR faults are embedded in the viscoelastic structure described in Stress and Seismicity Functions and Figure 4. Using $D=1.5$, Figure 16 shows the slip distributions resulting from the first 12 $M > 6.5$ events, and Figure 17 shows the corresponding stress levels just after termination of these events. Figure 18 shows time series of stress func-

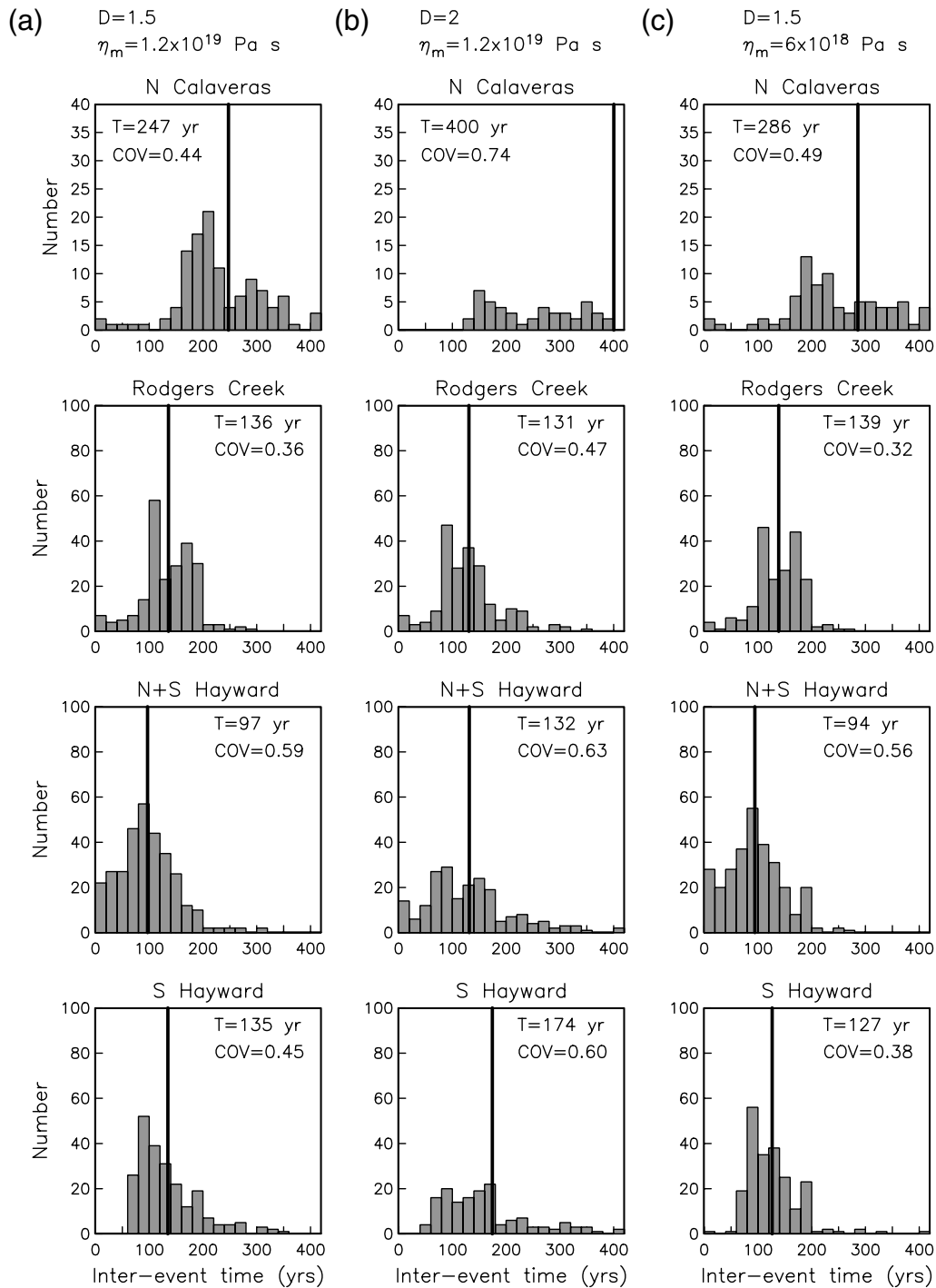


Figure 20. Histograms of interevent times of $M > 6.5$ events on four SFBR faults as a function of D and η_m . The histograms are binned in 20 yr time intervals. Mean recurrence interval (vertical black line segments) and coefficient of variation values are indicated.

tions CE, AS, and SD on four of the faults for the first 1000 yr. Several systematic patterns are evident: (1) shorter faults tend to saturate at smaller magnitudes (the largest earthquakes are smaller than those on relatively long faults); (2) on any given fault, the first ~ 100 yr of the model (i.e., from 2000 to 2100) tends to produce the largest events. The first large event on a given fault also tends to raise CE rather than lower it. Each of these features results from the arti-

ficially smooth initial stress distribution (Fig. 15), which prescribes stress at a given fault location independently of distance along dip; and (3) times of elevated production rate of moderate earthquakes tend to coincide with relatively high values of CE, AS, and SD.

The third property suggests that the production rate of moderate earthquakes may be a useful indicator of elevated stress levels and hence a fault that is relatively late in its cycle

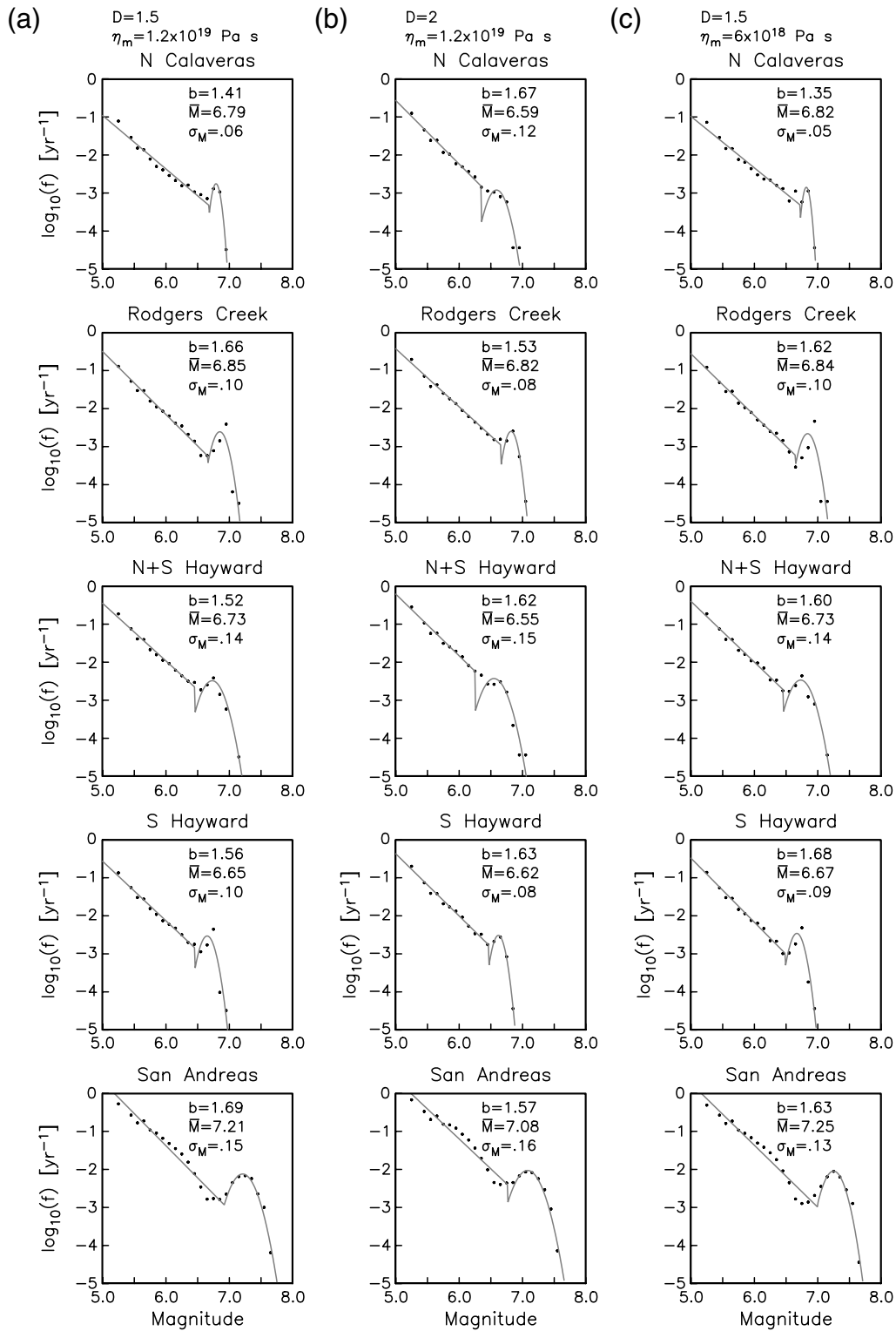


Figure 21. Frequency of earthquake occurrence on four SFBR faults as a function of D and η_m . Event frequency is compiled in bins of 0.1 magnitude unit. Superimposed for each distribution is the best-fitting curve given by equation (22). Best-fitting parameters $\{b, \bar{M}, \sigma_M\}$ are indicated.

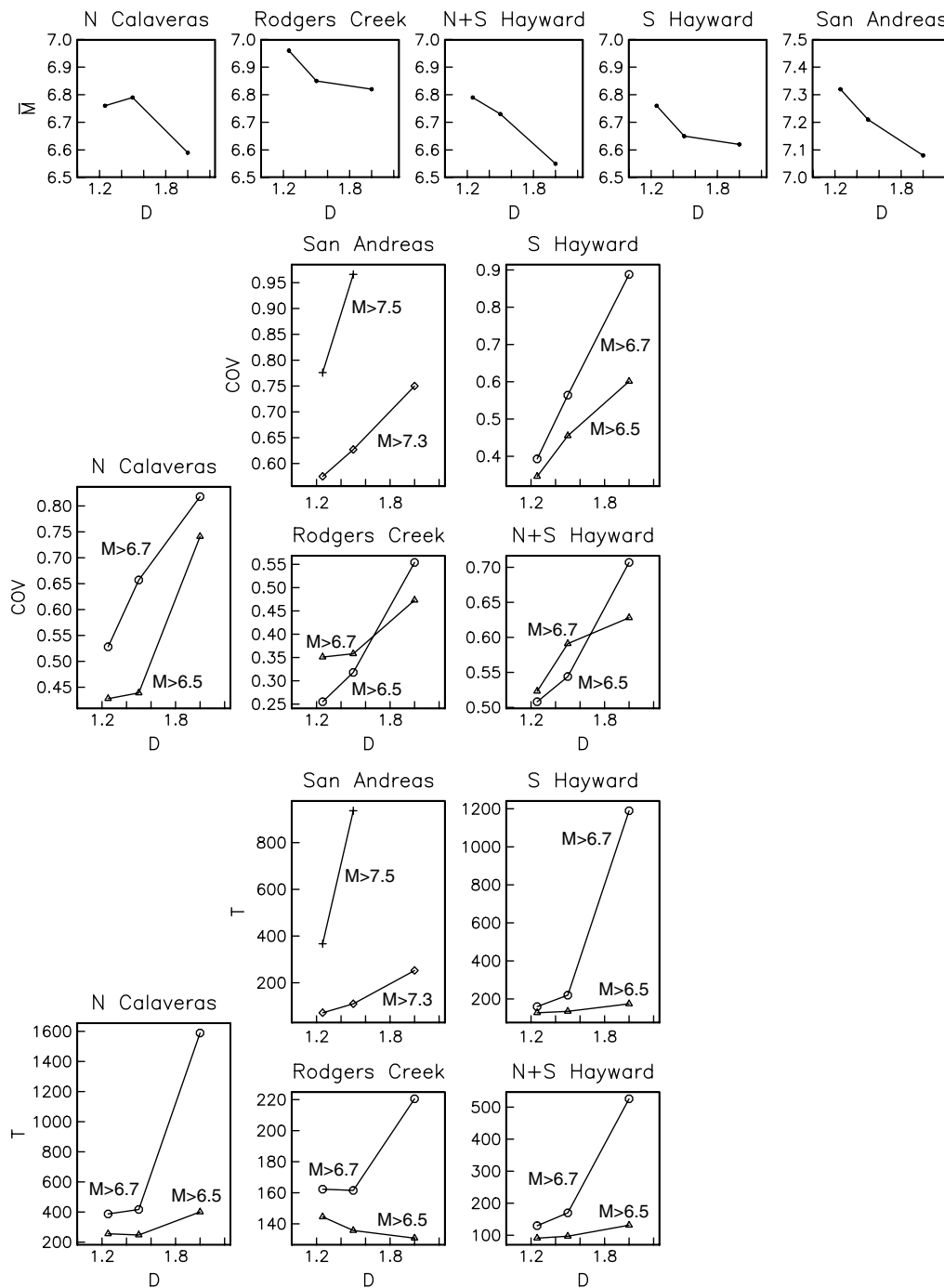


Figure 22. Mean recurrence interval T , coefficient of variation COV, and characteristic earthquake magnitude \bar{M} as a function of dynamic overshoot coefficient D on SFBR faults. Minimum magnitude is indicated for T and COV. Fixed $\eta_m = 1.2 \times 10^{19}$ Pa s is used in these simulations.

toward producing its next large earthquake. This is suggested by detailed consideration of the seismicity function FM (Fig. 19a). For example, taking the case $D = 1.5$ and $\eta_m = 1.2 \times 10^{19}$ Pa s, for a mainshock magnitude threshold of 6.5 the Rodgers Creek fault has a 13% probability of experiencing a mainshock within 14 yr of a moderate earthquake. The probability of an $M > 6.5$ mainshock occur-

ing within this time period by chance is given by equation (21) with $t = 14$ yr and $f = 7.38 \times 10^{-3}$ yr $^{-1}$ based on Figure 20 or Figure 21, yielding 10%. The same calculations for the southern Hayward fault yield a 12% probability of experiencing a mainshock within 14 yr of a moderate earthquake, compared with a 10% Poissonian probability.

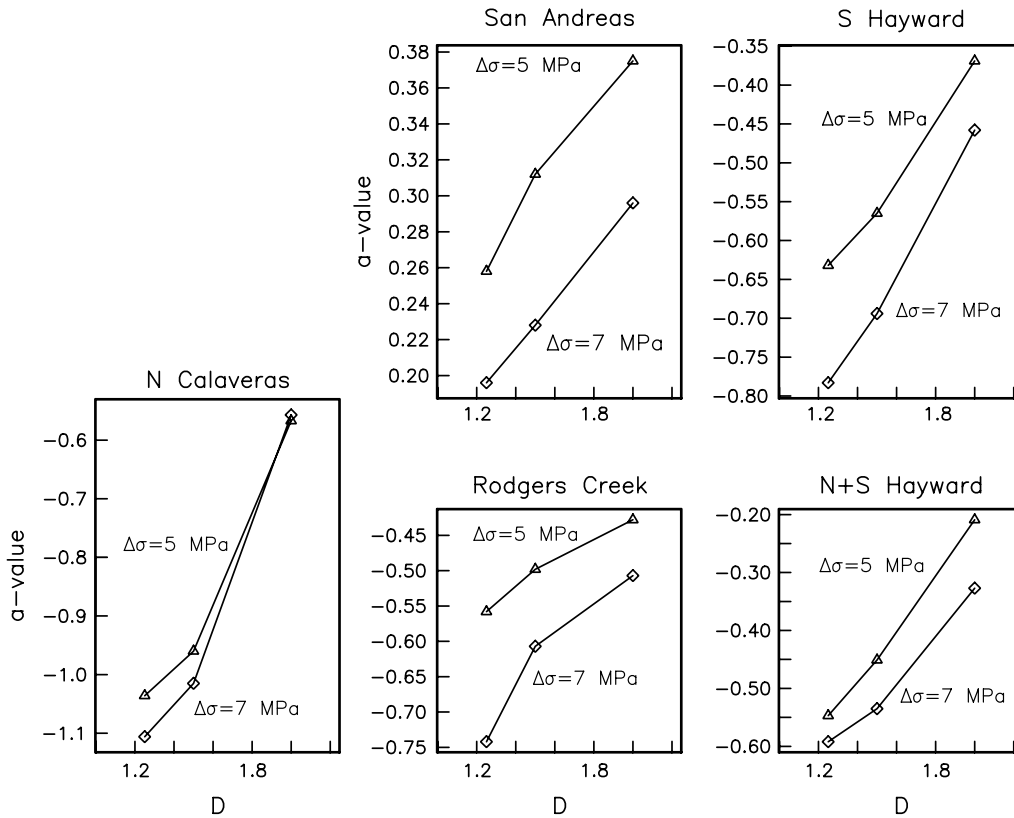


Figure 23. a -values on SFBR faults obtained in simulations as a function of D and $\Delta\sigma$.

Discussion

Magnitude-frequency statistics for the faults considered in both the 2-fault case (Fig. 11) and SFBR case (Fig. 21) generally exhibit two domains. At magnitudes ranging from 5 to about 6.8–7.5 (depending on fault length), the statistics obey a Gutenberg–Richter relationship with a b -value near 1.4. At larger magnitude the statistics are roughly Gaussian about a mean magnitude \bar{M} characteristic of the largest events that can occur on that fault. Wesnousky (1994) deduced such behavior for individual faults based on joint seismic and paleoseismic data. This behavior is qualitatively similar to the magnitude probability density function (PDF) employed by the Working Group on California Earthquake Probabilities (2003) in their figure 4.1. We quantify this PDF with a noncharacteristic PDF with slope $-b$ and a characteristic PDF:

$$\log_{10} f = \begin{cases} \log_{10} \left\{ \frac{\dot{N}(M^0) \beta \exp[-\beta(M-M^0)]}{1 - \exp[-\beta(M^u-M^0)]} \right\} & M < \bar{M} - 2\sigma_M \\ \log_{10} \left(c \exp \left\{ -\frac{1}{2} \left[\frac{(M-\bar{M})}{\sigma_M} \right]^2 \right\} \right) & M \geq \bar{M} - 2\sigma_M \end{cases}, \quad (22)$$

where $\beta = b \ln 10$ and c is a constant associated with the distribution of events of characteristic magnitude \bar{M} with Gaussian half-width σ_M . In equation (22) we follow Youngs and

Coppersmith (1985) in describing the noncharacteristic PDF as a truncated Gutenberg–Richter distribution with minimum magnitude M^0 , maximum magnitude M^u , and rate of earthquake production at magnitude above M^0 equal to $\dot{N}(M^0)$. We choose $M^u = \bar{M} - 2\sigma_M$ and $M^0 = 5.0$. An observed magnitude-frequency distribution may be optimally fit for all constants by performing a grid search over \bar{M} and σ_M and, for each set of trial values, solving for $\dot{N}(M^0)$, b , c in a least-squares inversion. The values of optimal $\{\bar{M}, \sigma_M\}$ are summarized for each magnitude-frequency distribution in Figures 11 and 21.

The statistics of long-term seismicity depend on the tuning parameters of the model (Ben-Zion, 2001; Ben-Zion *et al.*, 2003). In the present study this includes the stress reduction $\Delta\sigma$, the dynamic overshoot parameter D , and the viscoelastic structure as parameterized by η_m . For the synthetic two-fault case, Figures 11, 12, and 13 explore the dependence of magnitude-frequency distribution, interevent time statistics, and foreshock–mainshock function, respectively, on D and η_m . At fixed η_m the impact of increasing D from 1.5 to 2 is to slightly decrease the frequency of large ($M \gtrsim 7.3$) events and simultaneously increase the number of moderate events around $M \sim 6.0$ – 6.4 (Fig. 11a,b); these changes are seen for both faults 1 and 2. However, COV changes in opposite senses, with COV on fault 1 increasing and COV decreasing on fault 2 as D increases. FM for both faults slightly decreases with increas-

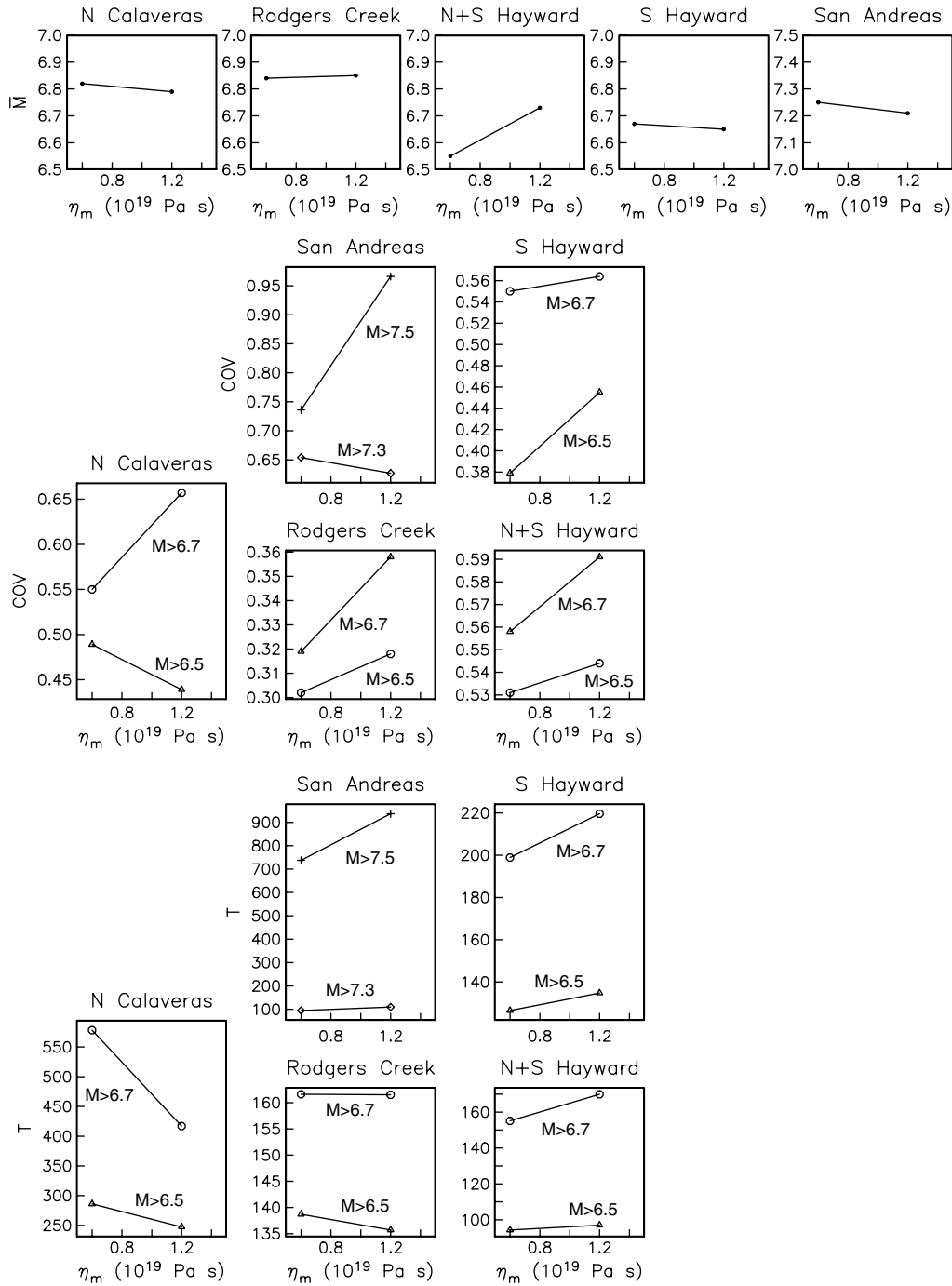


Figure 24. Mean recurrence interval T , coefficient of variation COV, and characteristic earthquake magnitude \bar{M} as a function of mantle viscosity η_m on SFBR faults. Minimum magnitude is indicated for T and COV. Fixed $D = 1.5$ is used in these simulations.

ing D because fewer large events occur at larger D (Fig. 13a,b).

A more consistent pattern is witnessed for FM, the interevent time statistics, and magnitude-frequency statistics for the SFBR system (Figs. 19–21). Increasing D tends to increase the interevent time and COV as well as diminish the characteristic magnitude \bar{M} (Fig. 22). Overall, the ratio of large events to small events diminishes as D increases. Similar behavior is witnessed in the Virtual

California simulations of Rundle *et al.* (2004, their figures 5 and 6) in which this ratio is found to increase as the level of dynamic weakening increases.

Figure 23 shows the a -values of the magnitude-frequency curves, that is, the intercept of the noncharacteristic PDF at M^0 given by

$$a = \log_{10} \left\{ \frac{\dot{N}(M^0)}{1 - \exp[-\beta(M^u - M^0)]} \right\}. \quad (23)$$

A decrease in D is always accompanied by a decrease in a -value. Taken together with the increase in \bar{M} with decreasing D (Fig. 22), this indicates that the slip budget at smaller D is accommodated by relatively fewer small and moderate magnitude events and a relatively greater number of large magnitude events.

In practically all cases considered (both two-fault and SFBR simulations), decreasing η_m at fixed D tends to decrease COV, resulting in a more regular occurrence of large earthquakes on a given fault (Figs. 12 and 20).

Figure 24 summarizes this behavior for the SFBR. This is tentatively rationalized by comparing the timescales of viscoelastic relaxation and large earthquake recurrence. Recurrence intervals in the various examples are typically 100 yr or greater. The mantle Maxwell relaxation times at $\eta_m = 1.2 \times 10^{19}$ Pa s and $\eta_m = 6 \times 10^{18}$ Pa s are 24 yr and 12 yr, respectively; the lower crust Maxwell relaxation times are 75% larger. These are the short-wavelength limits, and the relaxation times at wavelengths greater than the crustal thickness (e.g., a typical interfault spacing) are greater. The timescale of fault interaction produced by viscoelastic relaxation is thus of the same order as the interevent times for $\eta_m = 1.2 \times 10^{19}$ Pa s. Decreasing the viscosity by a factor of 2 apparently allows the dynamics of interseismic stressing to more efficiently decouple into a viscoelastic relaxation process and a steady/background stress buildup; for example, interfault communication occurs at timescales much less than a typical interevent time. Ben-Zion *et al.* (1993) suggest that the ratio between Maxwell relaxation time and elastic plate thickness, with units of inverse velocity, also controls the system behavior because this is comparable with the loading rate on the fault.

It is thought that the San Andreas fault SAF from Cape Mendocino to San Juan Bautista generates earthquakes of

magnitude ~ 7.8 quasiperiodically roughly every 300–400 yr (Working Group on California Earthquake Probabilities, 2003). The 1906 San Francisco earthquake had magnitude 7.8, average slip of about 5 m, and maximum slip of about 8 m (Thatcher *et al.*, 1997). The average slip needed to explain the geodetically measured coseismic deformation trades off with fault width and would be somewhat less using the 16 km fault width of the present study.) This behavior is mimicked in static cascade models of synthetic seismicity (Ward, 2000; Rundle *et al.*, 2006b). The earthquake model described here generates very long ruptures of magnitude $\gtrsim 7.6$ on the SAF much less frequently. The interevent time is $\gtrsim 10^4$ yr for all cases considered, and \bar{M} tends to be 7.5 or less on the SAF (Fig. 21). The maximum sized SAF event is of magnitude 7.6 or less, with neither average nor maximum slip exceeding 3 m using $\Delta\sigma = 5$ MPa (Fig. 25). The reasons for this include the use of a uniform distribution of stress reduction $\Delta\sigma$ and the choices of the values of $\Delta\sigma$ and D in the preceding simulations. The use of uniform $\Delta\sigma$ precludes the formation of asperities at fixed locations. As pointed out in Determination of Earthquake Ruptures, the average stress drop is generally less than $\Delta\sigma$, and this is the case for the SAF (Fig. 25). The stress drop lies between $\sigma - \sigma_a$ and $\sigma - \sigma_d$, where σ is the pre-event stress level. Large SAF ruptures typically propagate into low stress regions where σ is much smaller than σ_s , so that the mean stress drop of the event is generally only a fraction of $\sigma_s - \sigma_a = \Delta\sigma$. The slip and stress drop patterns in Figure 25 also confirm that with increasing D , cascade of a smaller event into a larger one is increasingly inhibited.

Because the models, which produce regular magnitude ~ 7.8 on the SAF (Ward, 2000; Rundle *et al.*, 2006b), use one-dimensional fault geometries (i.e., no discretization in depth) while the present simulations are discretized in depth, this

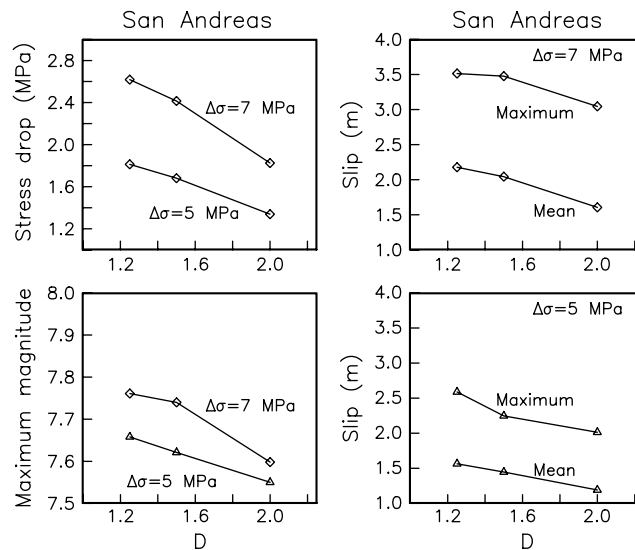


Figure 25. Maximum magnitude on the SAF and associated average stress drop, average slip, and maximum slip of the largest SAF event, obtained in simulations as a function of D and $\Delta\sigma$.

difference may partially contribute to the inability to produce large SAF events. The condition that stress drops not exceed 5 MPa in preceding simulations severely limits the achievable slip even in a long fault-rupture, and allowance for much greater stress drop, at least locally, must be a prerequisite for

producing long ruptures with average slip ~ 5 m and maximum slip $\gtrsim 8$ m. Figure 26 shows the magnitude-frequency statistics obtained by increasing $\Delta\sigma$ to 7 MPa, other factors being equal. Comparison with Figure 21 shows that this tends to raise \bar{M} by 0.05 to 0.2 magnitude units, depending

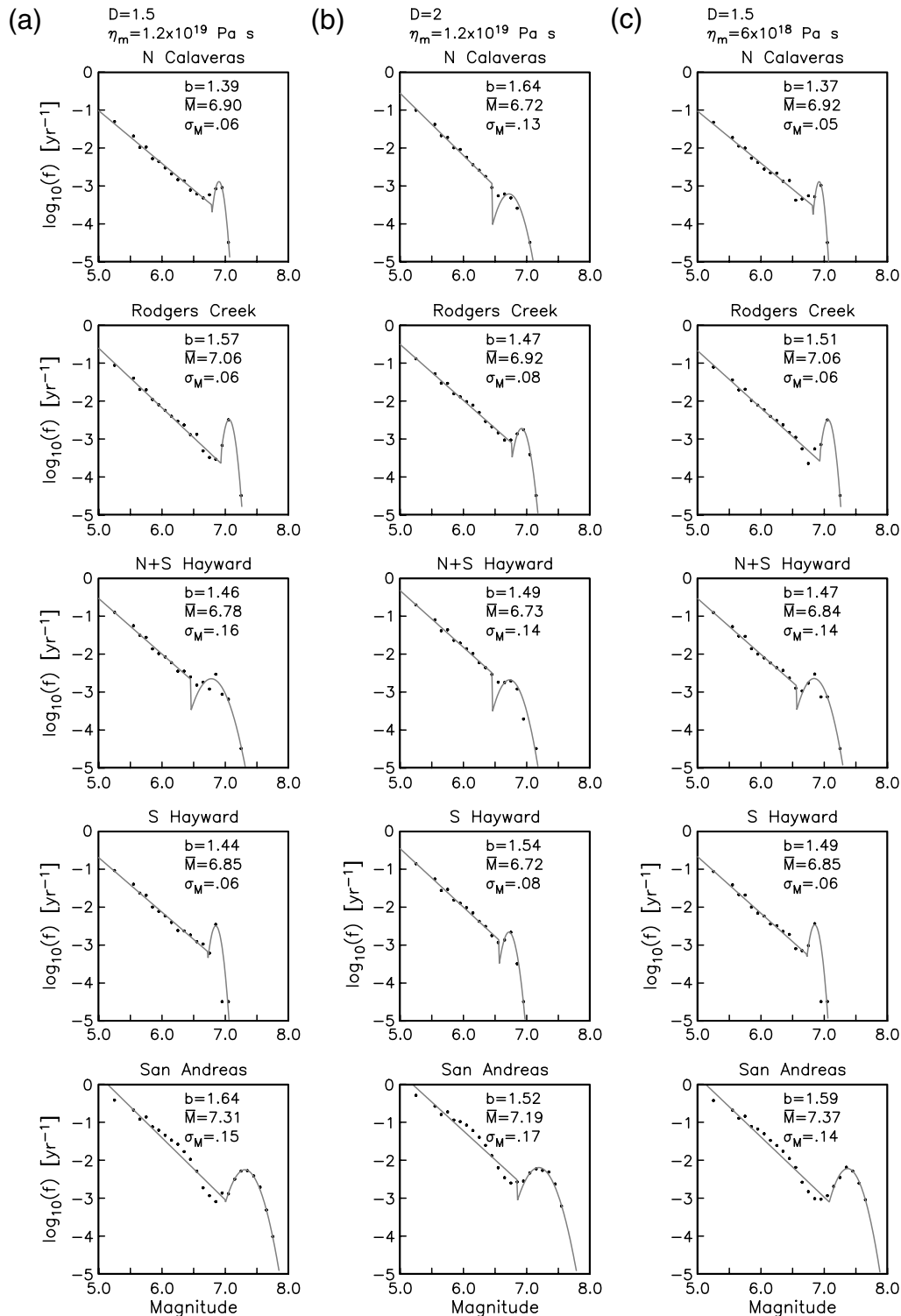


Figure 26. Same as Figure 21 except that $\Delta\sigma = 7$ MPa.

on other parameters. It still fails to produce events of magnitude ~ 7.8 (Fig. 25).

In addition to the SAF discrepancy, observed b -values for the SFBR as a whole are generally close to 1 (figure 4.5 of Working Group on California Earthquake Probabilities, 2003). Individual natural faults also tend to exhibit b -values close to 1 (Wesnousky, 1994). This is in contrast to b -values of 1.3–1.7 obtained for individual faults in present simulations. One mechanism for lowering b -value is to decrease D to values near 1, that is, allowing little fault healing during a rupture. This mechanism, which is suggested by comparing figures 7c,d of Ben-Zion *et al.* (2003) is found to be effective for reducing b -values on all regional faults to near 1 and raising the maximum magnitude of SAF events to about 7.8. An alternative solution for increasing the SAF mean characteristic magnitudes and lowering the b -values is to allow for strength heterogeneity. Inclusion of high-strength regions is generally expected to raise the maximum achievable slip on a given fault, and heterogeneous strength is known to be effective at broadening the range of magnitude-frequency statistics (e.g., Ben-Zion and Rice, 1993, 1995, 1997). On the other hand, for a given mean fault strength a limited range of strength heterogeneity is most effective in producing large ruptures on a smooth fault (e.g., the range of size scales parameter in section 5.2 of Ben-Zion, 2008), so that magnitude and b -value constraints on the SAF could place respective upper and lower bounds on the acceptable range of strength heterogeneity.

Conclusions

Statistical characterization of fault systems explored here are based on numerical simulations of seismicity over multiple fault cycles. The principal effects included in the 30,000 yr simulations are static stress transfer and viscoelastic stress transfer, which are implemented in the context of several interacting finite faults (finite in both length and width), including dipping faults.

Using a cascade approach to rupture initiation, propagation, termination, and postseismic adjustment, we explore the system behavior controlled by a few parameters. These include the stress reduction $\Delta\sigma$, a dynamic overshoot parameter D , which allows a degree of healing on fault patches while a synthetic rupture is underway, and the viscosity structure, which is represented by the mantle viscosity η_m , and which controls the rate of postseismic crustal stress adjustment. Although $\Delta\sigma$ determines the overall magnitude of ruptures, statistical properties of the system are controlled primarily by D and η_m . For example, magnitude-frequency patterns and COV are quite sensitive to both D and η_m . These results suggest that in a multifault system statistical behavior depends on the distribution of spatial scales (e.g., the relative lengths of the faults; their separation distances as a fraction of the depth to the relaxing lower crust) and temporal scales (the Maxwell relaxation times of the lower crust and mantle, the mean recurrence intervals on the faults).

Consistent patterns are obtained with respect to triggering capability of moderate events and the dependence of COV on model parameters. In both the two-fault and SFBR simulations, during a several-year period following a moderate event, the chance of a large event is $\sim 20\%$ – 30% more likely than the Poissonian probability of a large event occurring over the same length of time. COV tends to decrease with decreasing dynamic overshoot coefficient D , that is, large earthquake occurrence is more regular the greater the amount of dynamic weakening. COV also tends to decrease as the viscosity of the ductile substrate decreases. Because the characteristic earthquake magnitude also tends to increase as D decreases, the greater regularity of earthquakes for smaller D is, in part, the result of a greater proportion of earthquakes occurring in large magnitude events that release the stress built up over a long time interval; this is consistent with the smaller a values generally obtained for smaller D . The dependence of COV on η_m suggests that interaction of the different timescales involved in mantle relaxation and interevent times plays a role in shaping COV.

Producing large ($M \sim 7.8$) strike-slip ruptures on the San Andreas fault in the SFBR simulations is problematic using three-dimensional rupture mechanics, uniform frictional properties on all faults, and $\Delta\sigma \lesssim 7$ MPa; the same result holds on a simpler two-fault system involving very long parallel faults. These conditions also lead to magnitude frequency b -values on all faults considerably greater than 1. This suggests that either a large degree of dynamic weakening or substantial strength heterogeneity, likely involving local stress drops far exceeding 7 MPa, is a prerequisite for a cascade model to produce large strike-slip events and b -values close to those observed in nature. It is an open question whether these remedies, which are relevant to quasistatic mechanics, are sufficient to resolve these discrepancies or whether dynamic weakening mechanisms (e.g., thermal pressurization) in a dynamic rupture context are necessary.

Data and Resources

No data were used in this article. Some plots were made using Wessel and Smith's Generic Mapping Tools version 4.2.1 (www.soest.hawaii.edu/gmt, last accessed August 2008).

Acknowledgments

I am grateful to Jeanne Hardebeck and Morgan Page for internal reviews. This article benefitted from the constructive criticism of Roland Bürgmann, Yehuda Ben-Zion, and an anonymous reviewer.

References

- Ben-Zion, Y. (1996). Stress, slip, and earthquakes in models of complex single-fault systems incorporating brittle and creep deformations, *J. Geophys. Res.* **101**, 5677–5706.
- Ben-Zion, Y. (2001). Dynamic rupture in recent models of earthquake faults., *J. Mech. Phys. Solids* **49**, 2209–2244.

- Ben-Zion, Y. (2008). Collective behavior of earthquakes and faults: Continuum-discrete transitions, evolutionary changes and corresponding dynamic regimes, *Rev. Geophys.* **46**, doi 10.1029/2008rg000260.
- Ben-Zion, Y., and J. R. Rice (1993). Earthquake failure sequences along a cellular fault zone in a three-dimensional elastic solid containing asperity and nonasperity regions, *J. Geophys. Res.* **98**, 14109–14131.
- Ben-Zion, Y., and J. R. Rice (1995). Slip patterns and earthquake populations along different classes of faults in elastic solids, *J. Geophys. Res.* **100**, 12959–12983.
- Ben-Zion, Y., and J. R. Rice (1997). Dynamic simulations of slip on a smooth fault in an elastic solid, *J. Geophys. Res.* **102**, 17771–17784.
- Ben-Zion, Y., K. Dahmen, V. Lyakhovsky, D. Ertas, and A. Agnon (1999). Self-driven mode switching of earthquake activity on a fault system, *Earth Planet. Sci. Lett.* **172**, 11–21.
- Ben-Zion, Y., M. Eneva, and Y. Liu (2003). Large earthquake cycles and intermittent criticality on heterogeneous faults due to evolving stress and seismicity, *J. Geophys. Res.* **108**, 2307, doi 10.1029/2002JB002121.
- Ben-Zion, Y., J. R. Rice, and R. Dmowska (1993). Interaction of the San Andreas fault creeping segment with adjacent great rupture zones, and earthquake recurrence at Parkfield, *J. Geophys. Res.* **98**, 2135–2144.
- Feltzer, K. R., R. Abercrombie, and G. Ekström (2004). A common origin for aftershocks, foreshocks, and multiplets, *Bull. Seismol. Soc. Am.* **94**, 88–98.
- King, G. C., R. S. Stein, and J. Lin (1994). Static stress changes and the triggering of earthquakes, *Bull. Seismol. Soc. Am.* **84**, 935–954.
- Lyakhovsky, V., Y. Ben-Zion, and A. Agnon (2001). Earthquake cycle, fault zones, and seismicity patterns in a rheologically layered lithosphere, *J. Geophys. Res.* **106**, 4103–4120.
- Pollitz, F. F. (1996). Coseismic deformation from earthquake faulting on a layered spherical earth, *Geophys. J. Int.* **125**, 1–14.
- Pollitz, F. F. (1997). Gravitational viscoelastic postseismic relaxation on a layered spherical earth, *J. Geophys. Res.* **102**, 17921–17941.
- Pollitz, F. F. (2001). Viscoelastic shear zone model of a strike-slip earthquake cycle, *J. Geophys. Res.* **106**, 26541–26560.
- Pollitz, F. F., and M. C. J. Nyst (2004). A physical model for strain accumulation in the San Francisco Bay Region, *Geophys. J. Int.* **160**, 302–317.
- Pollitz, F. F., and D. S. Schwartz (2008). Probabilistic seismic hazard in the San Francisco Bay area based on a simplified viscoelastic-cycle model of fault interactions, *J. Geophys. Res.* **113**, B05409, doi 10.1029/2007JB005227.
- Richards-Dinger, K., and J. Dieterich (2007). Earthquake occurrence in regional-scale fault models with rate- and state-dependent friction, *EOS* **88**, no. 52, Fall Meet. Suppl., abstract S21C–0719.
- Rundle, J. B., P. B. Rundle, A. Donnellan, and G. Fox (2004). Gutenberg–Richter statistics in topologically realistic system-level earthquake stress-evolution simulations, *Earth Planets Space* **56**, 761–771.
- Rundle, J. B., P. B. Rundle, A. Donnellan, P. Li, D. L. Turcotte, R. Shcherbakov, P. Li, B. D. Malamud, L. B. Grant, G. C. Fox, D. McLeod, G. Yakovlev, J. Parker, W. Klein, and K. F. Tiampo (2005). A simulation-based approach to forecasting the next great San Francisco earthquake, *Proc. Nat. Acad. Sci.* **102**, 15363–15367.
- Rundle, J. B., P. B. Rundle, A. Donnellan, P. Li, W. Klein, G. Morein, D. L. Turcotte, and L. Grant (2006a). Stress transfer in earthquakes, hazard estimation and ensemble forecasting inferences from numerical simulations, *Tectonophysics* **413**, 109–125.
- Rundle, J. B., P. B. Rundle, K. F. Tiampo, A. Donnellan, and D. L. Turcotte (2006b). Virtual California: Fault model, frictional parameters, applications, *Pure Appl. Geophys.* **163**, 1819–1846.
- Savage, J. C. (1983). A dislocation model of strain accumulation and release at a subduction zone, *J. Geophys. Res.* **88**, 4984–4996.
- Savage, J. C. (2000). Viscoelastic-coupling model for the earthquake cycle driven from below, *J. Geophys. Res.* **105**, 25525–25532.
- Savage, J. C., and W. H. Prescott (1978). Asthenospheric readjustment and the earthquake cycle, *J. Geophys. Res.* **83**, 3369–3376.
- Shaw, B. E., and J. R. Rice (2000). Existence of continuum complexity in the elastodynamics of repeated fault ruptures, *J. Geophys. Res.* **105**, 23791–23810.
- Stein, R. S. (1999). The role of stress transfer in earthquake triggering, *Nature* **402**, 605–609.
- Thatcher, W., G. Marshall, and M. Lisowski (1997). Resolution of fault slip along the 470 km long rupture of the great 1906 San Francisco earthquake and its implications, *J. Geophys. Res.* **102**, 5353–5367.
- Ward, S. N. (2000). San Francisco Bay area earthquake simulations: A step toward a standard physical earthquake model, *Bull. Seismol. Soc. Am.* **90**, 370–386.
- Ward, S. N., and S. D. B. Goes (1993). How regularly do earthquakes recur? A synthetic seismicity model for the San Andreas fault, *Geophys. Res. Lett.* **20**, 2131–2134.
- Wesnousky, S. G. (1994). The Gutenberg–Richter or characteristic earthquake distribution, which is it? *Bull. Seismol. Soc. Am.* **84**, 1940–1959.
- Working Group on California Earthquake Probabilities (2003). Earthquake probabilities in the San Francisco Bay region, *U.S. Geol. Surv. Open-File Rept.* 03-214.
- Youngs, R., and K. Coppersmith (1985). Implications of fault slip rates and earthquake recurrence models to probabilistic seismic hazard estimates, *Bull. Seismol. Soc. Am.* **75**, 939–964.

USGS
Menlo Park, California

Manuscript received 27 August 2008